

Effect of Ni²⁺ substitution on the Structural, Magnetic and Dielectric Properties of PbFe_{12-x}Ni_xO₁₉ Nanoparticles

seyed ebrahim Mousavi Ghahfarokhi (✉ musavi_ebrahim@yahoo.co.uk)

Department of Physics, Faculty of Science, Shahid Chamran University of Ahvaz, Ahvaz, Iran
<https://orcid.org/0000-0002-4495-5859>

Foruzan Bazdar

Department of Physics, Faculty of Science, Shahid Chamran University of Ahvaz, Ahvaz, Iran

Iraj Kazeminezhad

Department of Physics, Faculty of Science, Shahid Chamran University of Ahvaz, Ahvaz, Iran

Elham Mohammadzadeh Shobegar

Department of Physics, Faculty of Science, Shahid Chamran University of Ahvaz, Ahvaz, Iran

Research Article

Keywords: PbFe_{12-x}Ni_xO₁₉ nanoparticles, Ni²⁺ substitution, Structural properties, Dielectric properties, Magnetic properties

Posted Date: September 14th, 2020

DOI: <https://doi.org/10.21203/rs.3.rs-74828/v1>

License:  This work is licensed under a Creative Commons Attribution 4.0 International License.

[Read Full License](#)

Effect of Ni²⁺ substitution on the structural, magnetic and dielectric properties of PbFe_{12-x}Ni_xO₁₉ nanoparticles

S.E. Mousavi Ghahfarokhi*, F. Bazdar, I. Kazeminezhad and E. Mohammadzadeh Shobegar

Department of Physics, Faculty of Science, Shahid Chamran University of Ahvaz, Ahvaz, Iran

Abstract

PbFe_{12-x}Ni_xO₁₉ nanoparticles (x = 0-1) were prepared by a sol-gel method. The influence of Ni²⁺ substitution on structural, magnetic and dielectric properties of PbFe₁₂O₁₉ nanoparticles was investigated. The samples of PbFe_{12-x}Ni_xO₁₉ nanoparticles have been characterized by the X-ray diffractometer (XRD), Fourier transform infrared spectrometer (FT-IR), scanning electron spectrometer (SEM), vibrating sample magnetometer (VSM), and an LCR meter. The results reveal that PbFe_{12-x}Ni_xO₁₉ compounds up to x = 0.2 are single phase. The bands of absorption in the 400–500 cm⁻¹ and the bands of absorption in the range of 500–600 cm⁻¹, corresponding to the formation of octahedral and tetrahedral sites which confirms the presence of metal–oxygen stretching band in ferrites. Also, SEM images show that by increasing Ni²⁺ doping grains size have been increased. However, for x > 0.2, the secondary Ni spinel ferrite (NiFe₂O₄) appears which the saturation magnetization and magnetic coercivity decreases. In addition, Ni²⁺ substitution reduces the dielectric constant, dielectric loss, and ac electrical conductivity for all samples decrease rapidly with increasing applied field frequency and reaches a constant value beyond a certain frequency which this is characteristic of the normal dielectric behaviour of ferrites and has been investigated by Maxwell–Wagner's two-layer model and Koop's theory. The variation in ac conductivity (σ_{ac}) with frequency shows that the electrical conductivity in these ferrites is mainly attributed to the electron hopping mechanism. Therefore; all single-phase Ni²⁺ substituted samples are suitable for use in magnetic recording media and microwave devices.

Keywords: PbFe_{12-x}Ni_xO₁₉ nanoparticles, Ni²⁺ substitution, Structural properties, Dielectric properties, Magnetic properties

* Corresponding author: Tel/Fax: +986133331040; E-mail address: musavi_ebrahim@yahoo.co.uk

1. Introduction

Recently, increasing attention has been paid to magnetic nanoparticles because of their wide application in industry and technology [1]. Magnetic hexaferrites have been used for many years. Among them, M-type hexaferrite has attracted more attention than others because of its application in permanent magnet, microwave devices, and high-density magnetic recording media, particularly for perpendicular magnetic recording [2-4]. In addition, these materials are well known because of excellent chemical stability, corrosion resistivity, large saturation magnetization and magnetic coercivity, high Curie temperature, good thermal durability, and mechanical hardness [5-10]. In recent years, many attempts have been made to enhance the structural, dielectric and magnetic properties of lead hexaferrite. One such attempt was to use the substitution of cations such as Cr^{3+} , Al^{3+} , Ga^{3+} , and Co^{2+} for Fe^{3+} sites of hexaferrites to enhance the above mentioned properties [7,11,12]. These substitutions strongly affect the structural, magnetic, and dielectric properties of hexaferrites [13]. The dielectric and magnetic properties of hexaferrites depend on the method of preparation, composition, and distribution of the substituted cations on the five crystallographic sites [14]. The effect of frequencies on the electrical behavior offers much valued information about the charge carriers which in turn helps to explicate the mechanisms responsible for charge transport phenomena and its dielectric behavior [15]. Since magnetic properties such as the saturation magnetization, the magnetic coercivity, and the magnetic anisotropy are related to the arrangement of cations in the hexagonal structure of the magnetoplumbite type, many studies have been performed on the substitution of cations in the hexaferrite structure. In addition to the chemical composition, particle size, shape, and method of hexaferrite fabrication affect its magnetic properties, and some researchers have investigated the effect of these parameters. For example, Albanese et al., synthesized, [16] magnetic and mossbauer measurements have been performed on polycrystalline samples of Ga substituted M-type hexagonal ferrites having compositions $\text{PbFe}_{12-x}\text{Ga}_x\text{O}_{19}$ ($0 < x < 11$). They found that the saturation magnetization (σ_s) at 0 K falls with increasing x , from $20 \mu_B$ for $x = 0$ to $4.32 \mu_B$ for $x = 6$. Guerrero-Serrano et al [17] reported the synthesis and study of the Lanthanum substitution in the lead M-Type Hexaferrite. They observed that the fall of two orders of magnitude in the magnetic coercivity is associated to the change of valence states of the iron cations located nearby of the lanthanum ions due to the substitution. M-type hexaferrites having a general formula $\text{MFe}_{12}\text{O}_{19}$ that where, M represents a divalent ion such as Ba^{2+} , Sr^{2+} or Pb^{2+} . It has hexagonal structure composed of stacked spinel ionic layers with interspaced ionic layers of M^{2+} , O^{2-} , and Fe^{3+} . The

divalent ion, M^{2+} , is substituted for an oxygen atom at every fifth layer, the Fe^{3+} ions are distributed on five different crystallographic sites and closed-packed oxygen layers stacked along the hexagonal c-axis [12, 18]. Ni is a good candidate for the substitution of Fe in lead hexaferrites due to similar ionic radii and electronic configuration of Ni and Fe [19]. Many preparation conditions have been developed to synthesize nanoparticles of M-type hexaferrite, such as compositions, annealing temperatures and times, atmospheres, types and quantities of dopants, heat treatment, and different preparation methods, including co-precipitation, glass crystallization, and the sol-gel methods [2,20]. In the present work, we report the synthesis and characterization of the structural, magnetic, and dielectric properties of Ni^{2+} substituted lead hexaferrite nanoparticles prepared by a sol-gel method.

2. Experimental Section

2.1. Synthesis

The nanoparticles composition of $PbFe_{12-x}Ni_xO_{19}$ (where $x = 0, 0.1, 0.2, 0.3, 0.4, 0.5, 0.6, 0.7, 0.8, 0.9, 1$) chemical were synthesized by the sol-gel method. The chemicals used for the preparation of the samples were $Fe(NO_3)_3 \cdot 9H_2O$, $Ni(NO_3)_2 \cdot 6H_2O$, and $Pb(NO_3)_2$ and were dissolved in 150 ml of de-ionized water. Citric acid was added to the solution, and the molar ratio for the metallic mixture to acid was kept at 1:1. The pH value of the solution was adjusted to 7 with addition gradual NH_3 . The obtained solution was heated using a hot plate on 80 °C with stirring until forming the gel. Then prepared gel was dried at temperature of 90 °C and time of 24 h in a oven of electric. The dry-gel was heated in afurnace in air atmosphere at a temperature 800 °C for 3 h.

2.2 Characterization

Thermo gravimetry (TGA: LINSEIS STA - PT1600) was carried out with a heating rate of 10 °C/min at ambient atmosphere. The prepared samples were examined by XRD using a Philips diffractometer (PW-1840) using Cu $K\alpha$ radiation wavelength of $\lambda = 1.54056 \text{ \AA}$, and field emission scanning electron microscope (FESEM) (FESEM Hitachi- S-4160). The FT-IR studies have been performed on a Perkin Elmer spectrometer (model BOMEN/MB102) with KBr pellet technique in the range of 400-4000 cm^{-1} . The magnetic properties were measured using a VSM (AGFM/VSM 3886) in a magnetic field strength of ± 15 kOe at room temperature. To investigate the dielectric properties of the samples such as the parallel capacity (C_p) and the parallel resistance (R_p), an LCR-meter (model: 8110 G) was used in the frequency range of 1 KHz to 1 MHz.

3. Results and discussion

3.1. Structural properties

The curves TGA / DTA of dry- gel precursor of $\text{PbFe}_{12-x}\text{Ni}_x\text{O}_{19}$ nanoparticles with $x = 0.0, 0.2,$ and 0.6 are shown in Fig. 1(a)-1(c), respectively. From TGA curves of Fig. 1, one can see that during the heat treatment, several processes occur on samples such as dehydration, decomposition, combustion and weight loss. Also, the TGA curves of Fig. 1 show that the four step of weight loss. The first step at temperature range $50 - 180\text{ }^\circ\text{C}$ is due to evaporation of water and volatile organic compounds in the sample. The second step of weight loss at temperature range about $180 - 250\text{ }^\circ\text{C}$ is mainly caused by the burning of citric acid, nitrates and organic compounds in the sample. The third step of weight loss at temperature range $250 - 450\text{ }^\circ\text{C}$ (Consistent with XRD results) is due to formation of hematite ($\alpha\text{-Fe}_2\text{O}_3$). The fourth step at temperature range $450 - 1000\text{ }^\circ\text{C}$, a very low weight loss has been observed that is due to the gradual elimination of impurities and formation lead hexaferrite phase [21]. The DTA curve in the pure sample has three endothermic peaks at temperatures of $86, 125$ and $161\text{ }^\circ\text{C}$, which relate to the evaporation of residual water and the organic compounds present in the sample. Three exothermic peaks are observed at temperatures of $215, 266$ and $534\text{ }^\circ\text{C}$. The exothermic peak at $215\text{ }^\circ\text{C}$ is caused by the burning of citric acid and the reaction between metal nitrates and citric acid. The exothermic peaks around $266\text{ }^\circ\text{C}$ are probably related to the onset of the formation of $\alpha\text{-Fe}_2\text{O}_3$ phase, and the peaks at $534\text{ }^\circ\text{C}$ are related to the onset of the formation of lead hexaferrites [22, 23]. The endothermic and exothermic peaks in Fig. 1(b) and 1 (c) which related to samples of $\text{PbFe}_{11.8}\text{Ni}_{0.2}\text{O}_{19}$ and $\text{PbFe}_{11.4}\text{Ni}_{0.6}\text{O}_{19}$ are almost the same as pure sample ($\text{PbFe}_{12}\text{O}_{19}$). In addition to the endothermic and exothermic peaks mentioned in the above, two exothermic peaks can be seen at temperatures of 934 and $950\text{ }^\circ\text{C}$ on the Fig. 1(b) and 1 (c) respectively, which it can be seen these peaks related to formation of $\text{PbFe}_{12-x}\text{Ni}_x\text{O}_{19}$ phases.

Fig. 2 shows the XRD patterns of $\text{PbFe}_{12-x}\text{Ni}_x\text{O}_{19}$ with $x = 0.0-1$ annealed at $800\text{ }^\circ\text{C}$ for 3 h. The indexed peaks on the XRD patterns of the lead hexaferrite phase ($\text{PbFe}_{12}\text{O}_{19}$), mono Ni ferrite phase (NiFe_2O_4), and hematite phase ($\alpha\text{-Fe}_2\text{O}_3$) in Fig. 2 corresponding to JCPDS card numbers 01-084-2046, 00-044-1485, and 01-072-0469, respectively. The reflection peaks with $2\theta \approx 30, 36, 43,$ and 63 corresponding to (220), (311), (400), and (440) planes of the NiFe_2O_4 . Also the reflection peaks with $2\theta \approx 33, 54,$ and 64 corresponding to (104), (116), and (300) planes of the $\alpha\text{-Fe}_2\text{O}_3$. Fig. 2 shows that, all samples of $\text{PbFe}_{12-x}\text{Ni}_x\text{O}_{19}$ up to $x = 0.2$ have the M-type lead ferrite hexagonal magnetoplumbite structure that is in agreement with JCPDS card number 01-084-2046. It seems that

the Fe^{3+} ions are substituted by Ni^{2+} ions [24] in the crystallographic sites of the $\text{PbFe}_{12}\text{O}_{19}$ structure. Also, changes in the intensity of peaks can be related to the occupation of the Ni^{2+} ions in the crystallographic sites. In contrast, for the $x > 0.2$ cases, the NiFe_2O_4 phase has been materialized in the samples. Also,

Fig. 2 show that by increasing Ni^{2+} substitution, the NiFe_2O_4 phase percent in the sample with $x = 1$ increases. The lattice constants (Eq. 1), unit cell volume (Eq. 2), X-ray density (Eq. 3), and average crystallites size (Eq. 4) for the samples with $x = 0-1$ are given in Table 1. The results of X-ray diffraction patterns show that by increasing Ni content the lattice parameter (c) decreases (Fig. 2), as the charge density of Ni^{2+} is lower than Fe^{3+} , therefore repulsion of Ni^{2+} ion by the adjacent ions in the lattice would be decreased. In order to minimize the repulsion and to maintain overall stability of the structure, the crystal structure condensed and as a result lattice parameter of c decreases [25]. Thus, by decreasing the constant c , the unit cell volume decreases. As the X-ray density is directly related with the molar mass of the sample (according to equation 3), therefore by increasing Ni (58.69 amu) substitution for Fe (55.85 amu), X-ray density of the Ni substituted samples increases [14, 26]. The average values of D were calculated in terms of the Scherer formula (Eq. 4). The D values of all samples much smaller than the critical size (270 nm) [27], so structure these samples are of the single-domain. The results reveal that the particles with single-domain structure and narrow size distribution can be prepared via the sol-gel method [28, 29].

Figs. 3 and 4 show that the FT-IR spectra of the $\text{PbFe}_{12-x}\text{Ni}_x\text{O}_{19}$ with $x = 0.0$ before annealing (dry-gel) and annealed samples with $x = 0.0, 0.2, 0.4,$ and 1 at temperatures of $800\text{ }^\circ\text{C}$ in the range $400-4000\text{ cm}^{-1}$, respectively. According to the Fig. 3, in the sample before annealing (dry-gel), band absorption in about of 3142.01 cm^{-1} indicates of the stretching vibration are attributed to water molecules O-H (water). The bands absorption in 1371.18 and 826.01 cm^{-1} , corresponding to stretching vibration bond NO_3 , which indicates the presence of nitric acid in the sample before annealing [30]. The bands absorption in $400-1000\text{ cm}^{-1}$, corresponding to the stretching vibration of the metal-oxygen (M-O). The bands of absorption in the $400-500\text{ cm}^{-1}$ and the bands of absorption in the range of $500-600\text{ cm}^{-1}$, corresponding to the formation of octahedral and tetrahedral sites which confirms the presence of metal-oxygen stretching band in ferrites. The vibration mode of tetrahedral clusters is higher as compared to that of octahedral clusters, which is due to the shorter band length of tetrahedral clusters [21]. The results of FT-IR spectra show that Ni^{2+} substitution is displaced bands

toward to the wave number less which these changes are due to large ionic radius and electro negativity of Ni^{2+} [19].

Fig. 5 shows the EDX pattern of $\text{PbFe}_{11.8}\text{Ni}_{0.2}\text{O}_{19}$ nanoparticles annealed at 800 °C for 3 h. It can be seen that there is no impurity element in the samples, which means that, the samples are not contaminated during the synthesis process. Of course, there are amounts of very low impurity elements such as Al and Au in the EDX pattern of $\text{PbFe}_{11.8}\text{Ni}_{0.2}\text{O}_{19}$ nanoparticles that these elements are due to preparation method of samples for measurement of SEM images. Because, usually from Al and Au elements for substrate and covering of the samples has been used.

The morphologies of the Ni^{2+} substituted hexaferrites samples were analysed by SEM. Fig.6 shows the SEM images of the $\text{PbFe}_{12-x}\text{Ni}_x\text{O}_{19}$ nanoparticles with $x = 0.0-1$ annealed at 800 °C for 3 h. The results of SEM prepared $\text{PbFe}_{12-x}\text{Ni}_x\text{O}_{19}$ with $x = 0.0-1$ show that nanoparticles shape for the samples up to $x = 0.4$ are spherical, and well-defined. Also, the results show that by increasing Ni doping grains size have been increased. The minimum average nanoparticles size (44 nm) is observed in the sample with $x = 0.2$.

3.2. Magnetic properties

Fig. 7 shows the M-H hysteresis loops of $\text{PbFe}_{12-x}\text{Ni}_x\text{O}_{19}$ samples with $x = 0.0-1$. The magnetic properties such as the saturation magnetization (M_s), the remanence magnetization (M_r), the magnetic coercivity (H_c), the squareness ratio (M_r/M_s), the crystalline anisotropy field (H_a),the magnetocrystalline anisotropy constant (K), and the demagnetization field (H_d) are given in Table 2. According to the results of Table 2 and Fig. 7, it is observed that by increasing Ni (x) doping, first at $x = 0.1$ the saturation magnetism decrease and then at $x = 0.2$ the saturation magnetization increases. The amount of Ni the saturation magnetization in the sample $x = 1$ (4.062 (emu /g)) decreases. In other words, the saturation magnetization values for $x = 0.2$ are higher than magnetization for other doping values.

Fig. 8 shows the saturation and the remanence magnetization as a function of Ni contents for samples of $\text{PbFe}_{12-x}\text{Ni}_x\text{O}_{19}$ with $x = 0.0-1$. Fig. 8 shows that by increasing Ni^{2+} substitution,the saturation and the remanence magnetization of samples have been decreased. The magnetic behaviors of M-type hexaferrite materials are largely governed by the distribution of iron ions in the crystal lattice sites such as three octahedral (2a, 12k, and 4f₂), one tetrahedral (4f₁) and one trigonal bipyramid (2b). It is know that the Ni^{2+} ion has a strong preference for octahedral site. As the magnetic moment of the Fe^{3+} ion ($5\mu_B$) is higher than of Ni^{2+} ion ($2\mu_B$); thus, by increasing Ni^{2+} substitution for the iron ions in the

sites having spins in the upward direction (12k, 2a), is expected to the total magnetic moment of the samples decrease and as a result the saturation and the remanence magnetization decreases [26,31,32].

Fig. 9 shows the magnetic coercivity, the crystalline anisotropy field and the demagnetization field as a function of Ni contents for $\text{PbFe}_{12-x}\text{Ni}_x\text{O}_{19}$ samples with $x = 0.0-1$. Fig. 9 shows that the magnetic coercivity, the crystalline anisotropy field, and the demagnetization field values of all samples decrease with increasing Ni^{2+} substitution. There are three reasons for reduce of H_c with increase Ni content. The first reason is the increase Ni spinel (NiFe_2O_4) by increasing Ni content. As the magnetic coercivity of NiFe_2O_4 is small as a result by increasing Ni content the magnetic coercivity of the Ni^{2+} substituted samples begins to decrease. The second reason for decrease of the magnetic coercivity is that the ionic radius of the Ni^{2+} (0.69 Å) is larger than of the Fe^{3+} (0.64 Å), so that the uniaxial anisotropy dose not remain along the easy c-axis; therefore, Ni^{2+} substitution changes the easy magnetization direction and as a result decreasing the anisotropy constant and the magnetic coercivity [22]. The third reason decrease of the magnetic coercivity with substitution of Ni^{2+} reduces in anisotropy that related to intrinsic effect associated with replacement of Fe^{3+} ions at both $4f_2$ and $2b$ sites. These two sites contribute to large magneto-crystalline anisotropy field [33]. Also, the crystalline anisotropy energy determines the easy magnetization direction in hexaferrite; therefore, Ni^{2+} substitution changes the easy magnetization direction and as a result decreasing the anisotropy constant (Fig. 10) [22]. In addition, it has been reported that a squareness ratio (M_r/M_s) at or above 0.5 indicates a magnetic domain below 0.5 is due to the formation of multi-domain structure. In this paper, the squareness ratio (M_r/M_s) is about 0.5, in the samples up to $x = 0.4$ which indicating these samples are in the single magnetic domain [34].

3.3. Dielectric properties

The dielectric properties of ferrites depends on factors such as types of charge carriers, which themselves depend on synthesis method, sintering conditions, chemical composition, ionic charge, and grain size. In this paper, the dielectric properties such as the dielectric constant (ϵ'), the dielectric loss (ϵ''), the ac conductivity (σ_{ac}), the magnetic permeability (μ'), the loss of magnetic permeability (μ''), and the inductance (L) were measured as a function of frequency in the frequency range of 1 KHz to 1 MHz with accuracy $\pm 5 \times 10^{-4}$ using an the inductance capacitance resistance (LCR) meter bridge.

Figs. 11 and 12 show the curves of the dielectric constant (ϵ') and the dielectric loss (ϵ'') as a function of applied frequency for all samples, respectively. From these curves, one can see that the both ϵ' and ϵ'' for all samples decrease rapidly by increasing applied field frequency and reach a constant value beyond a certain frequency. This is characteristic of the normal dielectric behaviour of ferrites, which has been investigated by Maxwell–Wagner’s two-layer model and Koop’s theory. The higher dielectric constant at low frequency is due to voids, dislocations, and other defects. Figs. 11 and 12 also show that the values of ϵ' and ϵ'' decrease by increasing Ni^{2+} substitutions. The behaviour of ϵ' and ϵ'' with Ni^{2+} substituted can be explained on the basis of the mechanism of dielectric polarization in ferrites which is similar to the process of electrical conduction. The values of the both ϵ' and ϵ'' of the $\text{PbFe}_{12-x}\text{Ni}_x\text{O}_{19}$ samples decrease due to the occupation of octahedral sites by Ni^{2+} ions [26]. Thus, the conduction mechanism in hexaferrite is the hopping of electrons at the octahedral sites. When the Ni^{2+} ions replace the iron ions at octahedral sites, the number of iron ions at octahedral site decrease as a result the hopping of electrons which are responsible for conductivity in the samples were reduced. Also, the values of ϵ' and ϵ'' decrease with Ni content, one can use these materials for applications in microwave devices [35, 36].

The real ac conductivity σ_{ac} consists of two terms:

$$\sigma = \sigma_1(T) + \sigma_2(\omega, T) \quad (19)$$

Where, σ_1 is the dc conductivity, which is dependent only on temperature, whereas σ_2 depends on both temperature and frequency and was calculated by the following formula [12]:

$$\sigma_2(\omega, T) = B(T) \omega^n(T) \quad (20)$$

Where, ω is the angular frequency, the parameter B has the units of conductivity, and the exponent n is non-dimensional.

The ac conductivity (σ_{ac}) values as a function of applied frequency and Ni contents for all samples are shown in Fig. 13 (a) and 13 (b) respectively. It can be seen from Fig. 13 (a) which by increasing frequency the ac conductivity decreases because, according to Koop’s model, the conductivity at low frequencies comes from the grain boundary which has a low conductivity. The conductivity at high frequency comes from the grains which have high ac conductivity. Fig. 13(b) shows that by increasing Ni contents the ac conductivity decreases because conduction mechanism in hexaferrite is the hopping of electrons at the octahedral sites. When the Ni^{2+} ions replace the iron ions at octahedral

sites, the number of iron ions at this site decrease as a result the hopping of electrons which are the ac conductivity value of the samples.

The plots of magnetic permeability (μ') as a function of applied frequency for all $\text{PbFe}_{12-x}\text{Ni}_x\text{O}_{19}$ with $x = 0.0-1$ are shown in Fig. 14 (a). The observed reduction in magnetic permeability at high frequency is due to an increase in vortical currents at high frequencies because; by increasing vortical currents applied magnetic field decrease as a result the magnetic permeability decreases. Fig. 14 (b) also shows that by increasing Ni^{2+} contents the magnetic permeability was reduced. Because, with substitute of $\text{Ni}^{2+}(2\mu_B)$ for Fe ($5\mu_B$) magnetic moment in the samples decrease. Also, by increasing Ni^{2+} contents the magnetic permeability of samples is slowly increased which this increase is due to presence Ni ferrite (NiFe_2O_4).

The plots of the loss of magnetic permeability (μ'') as a function of applied frequency for all $\text{PbFe}_{12-x}\text{Ni}_x\text{O}_{19}$ with $x = 0.0-1$ are shown in Fig. 15. Fig. 15 reveals that by increasing frequency the loss of magnetic permeability of samples were decreased which this reduces in high frequencies is normal behaviour of ferrites.

4. Conclusions

$\text{PbFe}_{12-x}\text{Ni}_x\text{O}_{19}$ samples with $x = 0.0-1$ were synthesized by a sol-gel method and the role of Ni^{2+} substitution on structure, magnetic and dielectric in the Lead hexaferrite nanoparticles have been investigated. The XRD measurements reveal that the structures of $\text{PbFe}_{12-x}\text{Ni}_x\text{O}_{19}$ samples up to $x = 0.2$ are single-phase, whereas a second phase (NiFe_2O_4) appears in the samples with $x > 0.2$. The SEM images of all samples show that by increasing Ni doping grains size were increased. The minimum average nanoparticles size (44 nm) is observed in the sample with $x = 0.2$. The reduction in the saturation and the remanence magnetization for high Ni^{2+} contents is mainly attributed to the decrease in molar magnetic moment by the substitution of Ni^{2+} ($\sim 2\mu_B$) for Fe^{3+} ($\sim 5\mu_B$). Also, the magnetic coercivity values of all samples decrease by increasing Ni content. The results of LCR meter measurements show that the values of ϵ' , ϵ'' , and σ_{ac} decrease by increasing Ni^{2+} contents. The variations in the dielectric constant and dielectric loss with frequency are discussed on the basis of the Maxwell- Wagner and Koop's theories. These observation suggests that papered samples in this research are suitable for applications in microwave devices. The observed reduction in magnetic permeability at high frequency is due to an increase in vortical currents at high frequencies.

Also, by increasing frequency the loss of magnetic permittivity of samples were decreased which this reduces in high frequencies is normal behaviour of ferrites.

Acknowledgments

The authors are grateful to ShahidChamranUniversity of Ahvaz for providing us with financial support for this project.

5. References

- [1] Spaldin, N. A.:Magnetic Materials: Fundamentals and Applications. 2nd ed. Cambridge University Press,Cambridge, New York,(2011)
- [2] Lin, C. R., Siao, Y. J., Hsieh, M. H.: Magnetic properties of lead ferrite nanoparticles prepared by the polymerized complex method. *J.Alloys Compd.***462**,315-319 (2008)
- [3] Hussain, S., Shah, N. A., Maqsood, Ali, A., Naeem, A. M., Ahmad, W., Adil Syed.:Characterization of Pb-doped Sr-Ferrites at Room Temperature. *Supercond. Nov .Magn.***24**,1245-1248 (2011)
- [4] Davoodi, A., Hashemi, B.:Magnetic properties of Sn–Mg substituted strontium hexaferrite nanoparticles synthesized via coprecipitation method. *J.Alloys Compd.* **509**,5893-5896 (2011)
- [5] Zi, J. Z. F., Sun, Y. P. , Zhu, X. B., Yang, Z. R. , Dai, J. M., Song,W. H., Structural and magnetic properties of SrFe₁₂O₁₉ hexaferrite synthesized by a modified chemical co-precipitation method. *J. Magn. Mater.* **320**, 2746-2751 (2008).
- [6] Ashiq , M. N., Iqbal, M. J., ul-Haq, M. N., Gomez, P.H., Qureshi, A. M.,Synthesis, magnetic and dielectric properties of Er–Ni doped Sr-hexaferrite nanomaterials for applications in High density recording media and microwave devices. *J. Magn. Mater.* **324**, 15-19 (2012).
- [7] Iqbal, M. J.,Ashiq , M. N., Gomez, P.H.,Effect of doping of Zr–Zn binary mixtures on structural, electrical and magnetic properties of Sr-hexaferrite nanoparticles. *J. Alloys Compd.* **478**, 736-740 (2009).
- [8] Wang ,Y. , Wang,Y.,Li,Q.,Zhang,C.,Li,B., Effect of Fe/Sr mole ratios on the formation and magnetic properties of SrFe₁₂O₁₉ microtubules prepared by sol–gel method. *J. Magn. Mater.* **321**, 3368-3372 (2009).

- [9] Ashiq, M. N., Iqbal, M. J., Gul, I. H., Effect of Al–Cr doping on the structural, magnetic and dielectric properties of strontium hexaferrite nanomaterials. *J. Magn. Magn. Mater.* **323**, 259-263 (2011).
- [10] Iqbal, M. J., Ashiq, M. N., Hernandez-Gomez, P., Munoz, J. M., Cabrera, C. T., Influence of annealing temperature and doping rate on the magnetic properties of Zr–Mn substituted Sr-hexaferrite nanoparticles. *J. Alloys Compd.* **500**, 113-116 (2010).
- [11] Iqbal, M. J., Ashiq, M. N.: Physical and electrical properties of Zr–Cu substituted strontium hexaferrite nanoparticles synthesized by co-precipitation method. *Chem. Eng. J.* **136**, 383-389 (2008)
- [12] Mousavi Ghahfarokhi, S. E., Ranjbar, F., Zargar Shoushtari, M.: A study of the properties of SrFe_{12-x}Co_xO₁₉ nanoparticles. *J. Magn. Magn. Mater.* **349**, 80-87 (2014)
- [13] Mozaffari, M., Arab, A., Yousefi, M. H., Amighian, J.: Preparation and investigation of magnetic properties of MnNiTi-substituted strontium hexaferrite nanoparticles. *J. Magn. Magn. Mater.* **322**, 2670-2674 (2010)
- [14] Iqbal, M. J., Ashiq, M. N., Gul, I. H., Physical, electrical and dielectric properties of Ca-substituted strontium hexaferrite (SrFe₁₂O₁₉) nanoparticles synthesized by co-precipitation method. *J. Magn. Magn. Mater.* **322**, 1720-1726 (2010)
- [15] Cernea, M., Negrea, R. F., Ciuchi, I. V., Baldisserri, C., Trusca, R., & Galassi, C., Dielectric characterization of Ba_xSr_{1-x}Fe₁₂O₁₉ (x=0.05–0.35) ceramics. *Ceram. Int.* **42**, 1050–1056 (2016)
- [16] Albanese, G., Leccabue, F., Watts, B. E., Magnetic and Mossbauer investigation of PbFe_{12-x}Ga_xO₁₉ hexagonal ferrites. *J. mater. sci.* **37**, 3759 – 3763 (2002)
- [17] Guerrero-Serrano, A. L., Mirabal-Garcia, M., Palomares-Sanchez, S. A., Synthesis and Study of the Lanthanum Substitution in the Lead M-Type Hexaferrite. *J Supercond Nov Magn.* **27**, 1709–1713 (2014)
- [18] Iqbal, M. J., Ashiq, M. N., Gomez, P.H., Munoz, J.M.: Synthesis, physical, magnetic and electrical properties of Al–Ga substituted co-precipitated nanocrystalline strontium hexaferrite. *J. Magn. Magn. Mater.* **320**, 881-886 (2008)
- [19] Vinnik, D., Zhrebtsov, D., Mashkovtseva, L., Nemrava, S., Semisalova, A., Galimov, D., Gudkova, S., Chumanov, I., Isaenko, L., and Niewa, R., Growth, structural and magnetic

characterization of Co- and Ni-substituted barium hexaferrite single crystals. *J. Alloys Compd.* **628**, 480-484 (2015).

[20] Mousavi Ghahfarokhi, S.E., Rostami, Z.A., Kazeminezhad, I.:Fabrication of $\text{PbFe}_{12}\text{O}_{19}$ nanoparticles and study of their structural, magnetic and dielectric properties. *J. Magn. Magn.Mater.* **399**, 130-142 (2016)

[21] Zargar Shoushtari, M., Ranjbar, F.,Mousavi Ghahfarokhi S. E.:Effect of calcination temperature and time on the structural and electrical properties of $\text{SrFe}_{12}\text{O}_{19}$ nanoparticles.Iranian J Phys Res. **14**,305-316 (2015)

[22] Iqbal, M. J., Farooq, S.:Impact of Pr–Ni substitution on the electrical and magnetic properties of chemically derived nanosized strontium–barium hexaferrites.*J.Alloys Compd.*, **505**, 560-567 (2010)

[23] Nga, T. T. V., Duong, N.P., Hien, T. D.:Synthesis of ultrafine $\text{SrLa}_x\text{Fe}_{12-x}\text{O}_{19}$ particles with high coercivity and magnetization by sol–gel method. *J.Alloys Compd.*, **475**,55-59(2009)

[24] Kittel,C.:Introduction to Solid State Physics. 8th Edition chapter 22 November(2004)

[25] Iqbal, M. J., Farooq, S.:Enhancement of electrical resistivity of $\text{Sr}_{0.5}\text{Ba}_{0.5}\text{Fe}_{12}\text{O}_{19}$ nanomaterials by doping with lanthanum and nickel.*Mater.Chem. Phys.* **118**,308-313 (2009)

[26] Ashiq,M.N., Iqbal, M. J., Najam-ul-Haq, M., Gomez, P.H., Qureshi, A.M.:Synthesis, magnetic and dielectric properties of Er–Ni doped Sr-hexaferrite nanomaterials for applications in High density recording media and microwave devices.*J. Magn. Magn.Mater.***324**, 15-19 (2012)

[27] Fang, Q.Q., Bao, H.W., Fang, D.M., Wang, J.Z.,Li, X.G.:The effect of Zn–Nb substitution on magnetic properties of strontium hexaferrite nanoparticles.*J. Magn. Magn.Mater.***278**, 122-126(2004)

[28] Yue, Z., Guo, W ., Zhou, J., Gui Z., and Li, L.: Synthesis of nanocrystalline ferritesby sol–gel combustion process: the influence of pH value of solution.*J. Magn. Magn.Mater.***270**, 216–223 (2004)

[29] Teh, G.B., Wong, Y. C., Tilley R.D.:Effect of annealing temperature on the structural, photoluminescence and magnetic properties of sol–gel derived Magnetoplumbite-type (M-type) hexagonal strontium ferrite. *J. Magn. Magn.Mater.***323**,2318-2322 (2011)

- [30] Singhal, S., Namgyal, T., Singh, J., Chandra, K., Bansal, S., A comparative study on the magnetic properties of $MFe_{12}O_{19}$ and $MAFe_{11}O_{19}$ (M= Sr, Ba and Pb) hexaferrites with different morphologies. *Ceram. Int.* **37**, 1833-1837 (2011).
- [31] Rane, M.V., Bahadur, D., Kulkarni, S.D., Date, S.K.: Magnetic properties of NiZr substituted barium ferrite. *J. Magn. Magn. Mater.* **195**, L256-L260 (1999)
- [32] Bercoff, P.G., Herme, C., Jacobo, S.E.: The influence of Nd–Co substitution on the magnetic properties of non-stoichiometric strontium hexaferrite nanoparticles. *J. Magn. Magn. Mater.* **321**, 2245-2250 (2009)
- [33] Suarez, G.M., Vazques, L.R., Huacuz, J.C.C., Fuentes, A.F., Egarcia, J.I.: Magnetic properties and microstructure of $BaFe_{11.6-2x}Ti_xM_xO_{19}$ (M=Co, Zn, Sn) compounds. *Physica B.* **339**, 110-118 (2003)
- [34] Liu, M.Q., Shen, X.Q., Song, F.Z., Xiang, J., Meng, X.F.: Microstructure and magnetic properties of electrospun one-dimensional Al^{3+} substituted $SrFe_{12}O_{19}$ nanofibers. *J. Solid State Chem.* **184**, 871-876 (2011)
- [35] Sindhu, S., Anantharaman, M.R., Thampi, B.P., Malini, K.A., Kurian, P.: Evaluation of a.c. conductivity of rubber ferrite composites from dielectric measurements. *Bull. Mater. Sci.* **25**, 599-607 (2002)
- [36] Ashiq, M.N., Iqbal, M.J., Gul, I.H.: Effect of Al–Cr doping on the structural, magnetic and dielectric properties of strontium hexaferrite nanomaterials. *J. Magn. Magn. Mater.* **323**, 259-263 (2011)

Figures

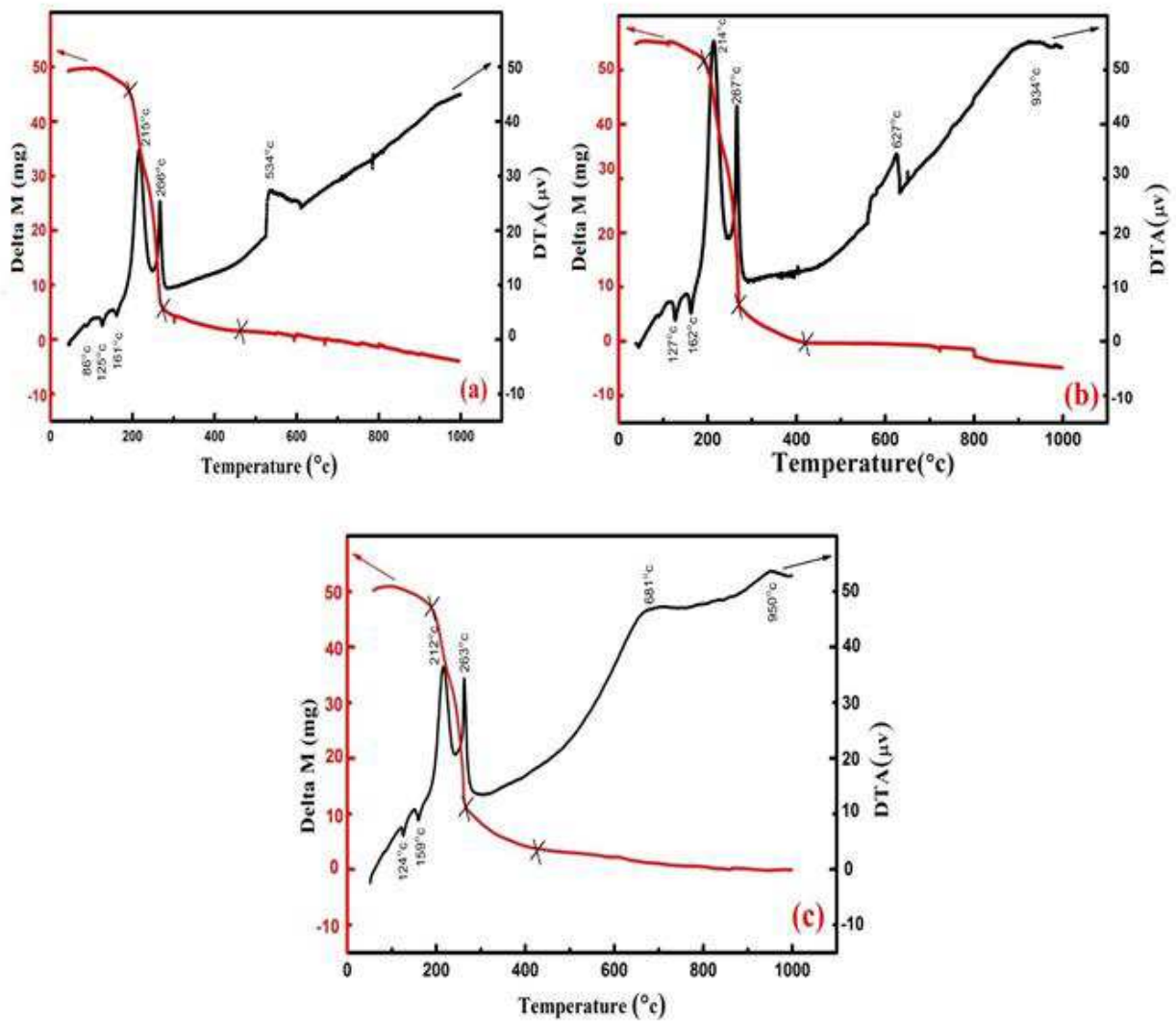


Fig. 1: TGA/DTA curves of the dry-gel precursor of $\text{PbFe}_{12-x}\text{Ni}_x\text{O}_{19}$ nanoparticles annealed at 800°C for 3 h with (a) $x = 0.0$; (b) $x = 0.2$ and (c) $x = 0.6$.

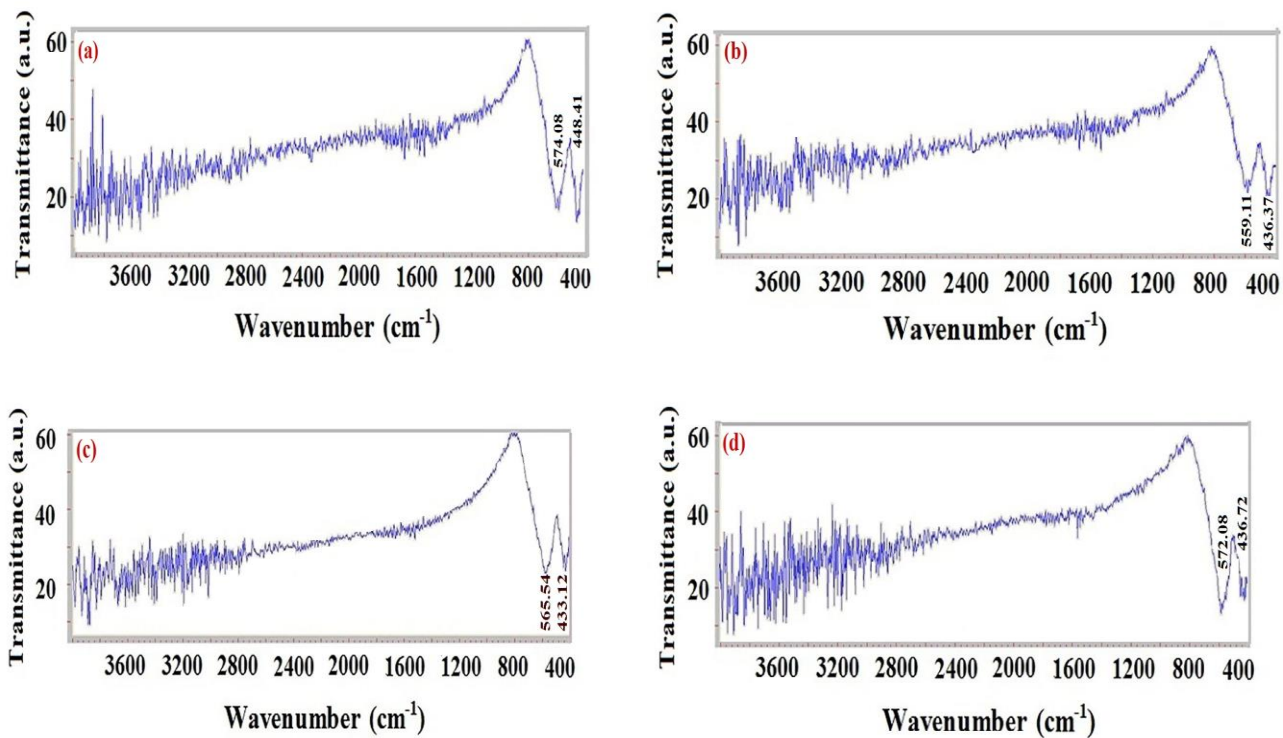


Fig. 4: FT-IR patterns of $\text{PbFe}_{12-x}\text{Ni}_x\text{O}_{19}$ nanoparticles annealed at $800\text{ }^\circ\text{C}$ for 3 h with (a) $x = 0.0$; (b) $x = 0.2$; (c) $x = 0.4$ and (d) $x=1$.

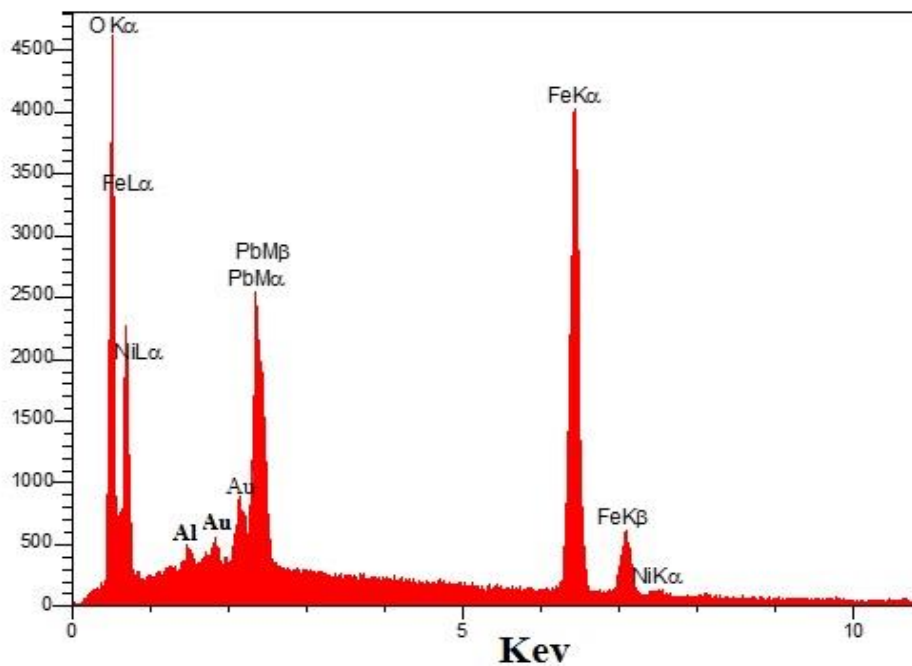


Fig. 5: EDX pattern of $\text{PbFe}_{11.8}\text{Ni}_{0.2}\text{O}_{19}$ nanoparticles annealed at $800\text{ }^\circ\text{C}$ for 3 h.

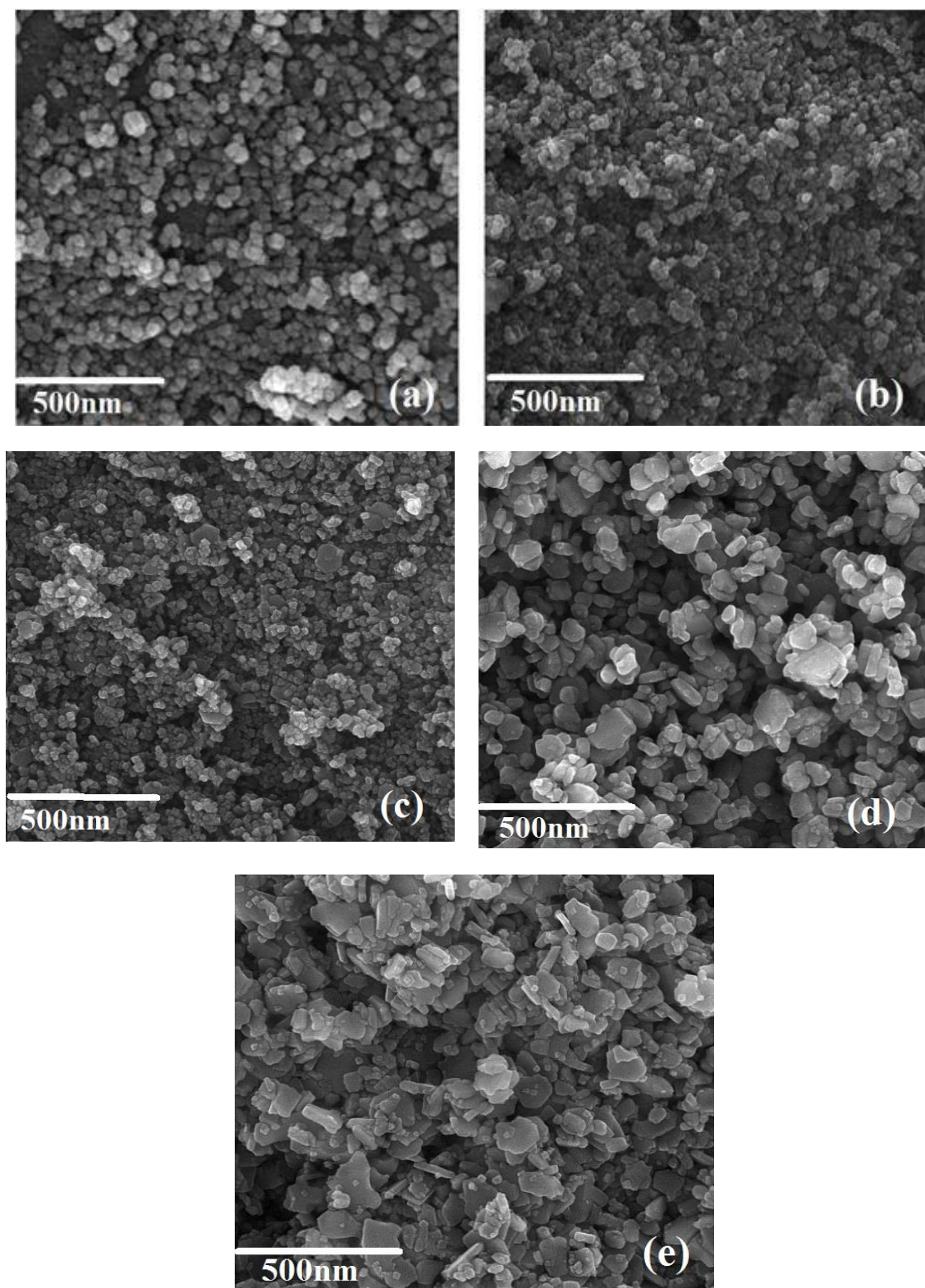


Fig. 6: SEM images of $\text{PbFe}_{12-x}\text{Ni}_x\text{O}_{19}$ nanoparticles annealed at $800\text{ }^\circ\text{C}$ for 3 h with (a) $x = 0.0$, (b) $x = 0.2$, (c) $x = 0.4$, (d) $x = 0.6$ and (e) $x = 1$.

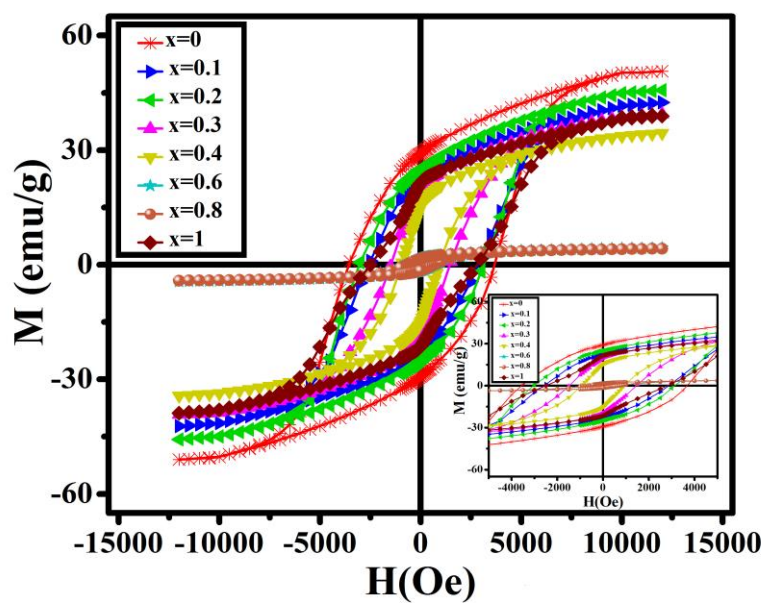


Fig. 7: M-H hysteresis loops of $\text{PbFe}_{12-x}\text{Ni}_x\text{O}_{19}$ nanoparticles annealed at $800\text{ }^\circ\text{C}$ for 3 h with $x = 0.0-1.0$.

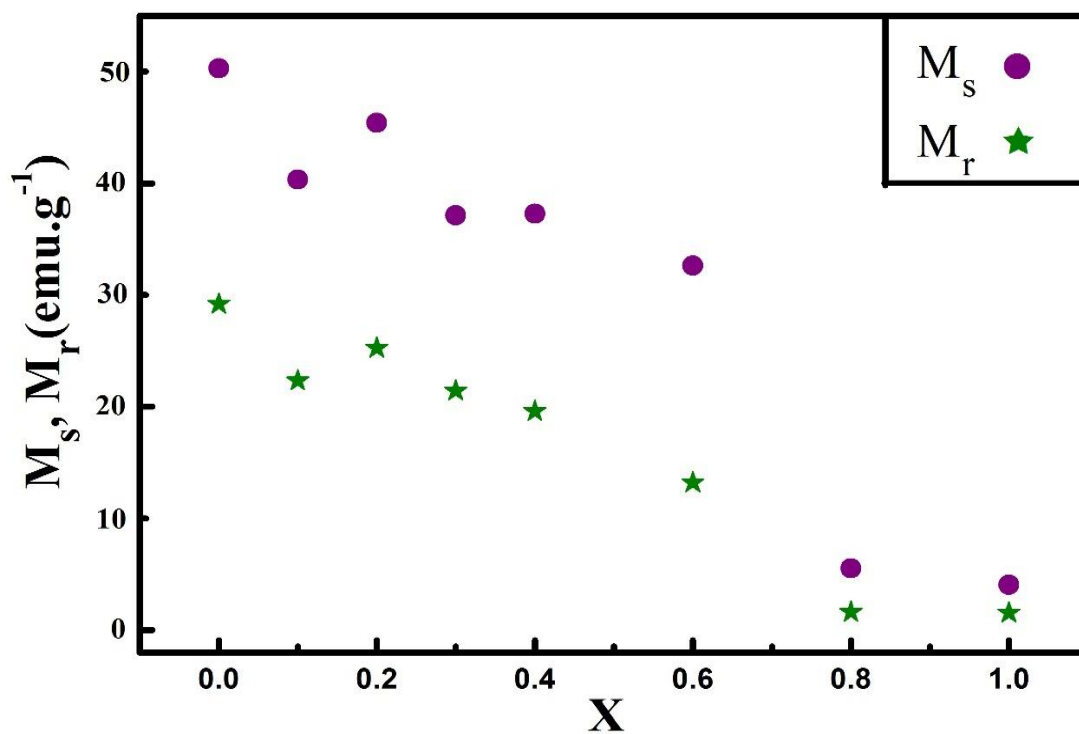


Fig. 8: The variations of M_s and M_r with respect to x values for $\text{PbFe}_{12-x}\text{Ni}_x\text{O}_{19}$ nanoparticles annealed at $800\text{ }^\circ\text{C}$ for 3 h.

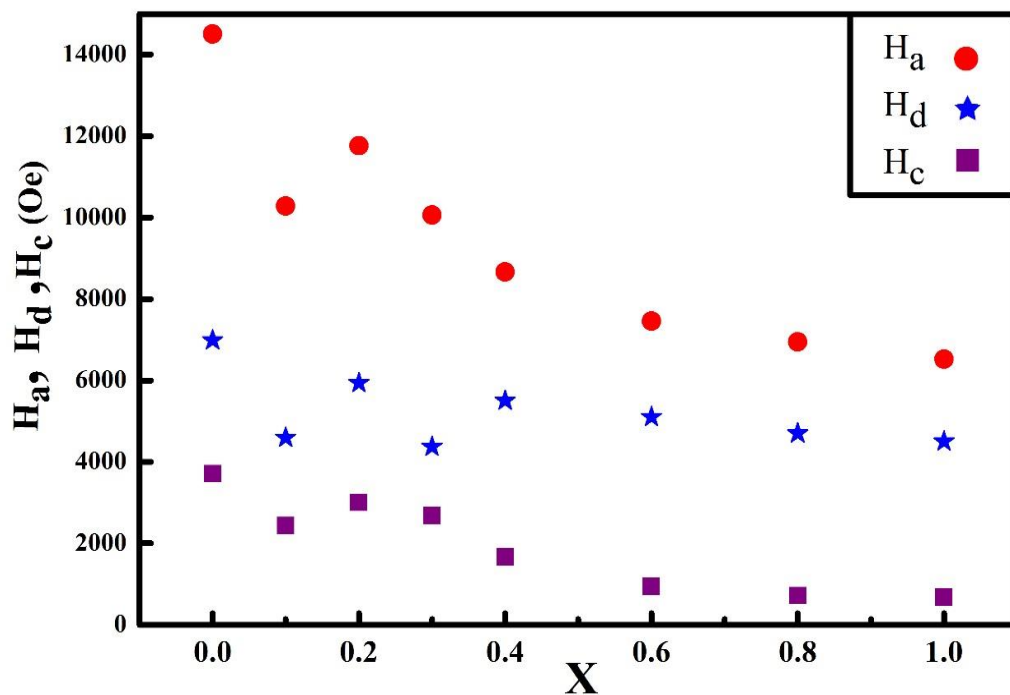


Fig. 9: The variations of H_c , H_a and H_d with respect to x values for $PbFe_{12-x}Ni_xO_{19}$ nanoparticles annealed at $800\text{ }^\circ\text{C}$ for 3 h.

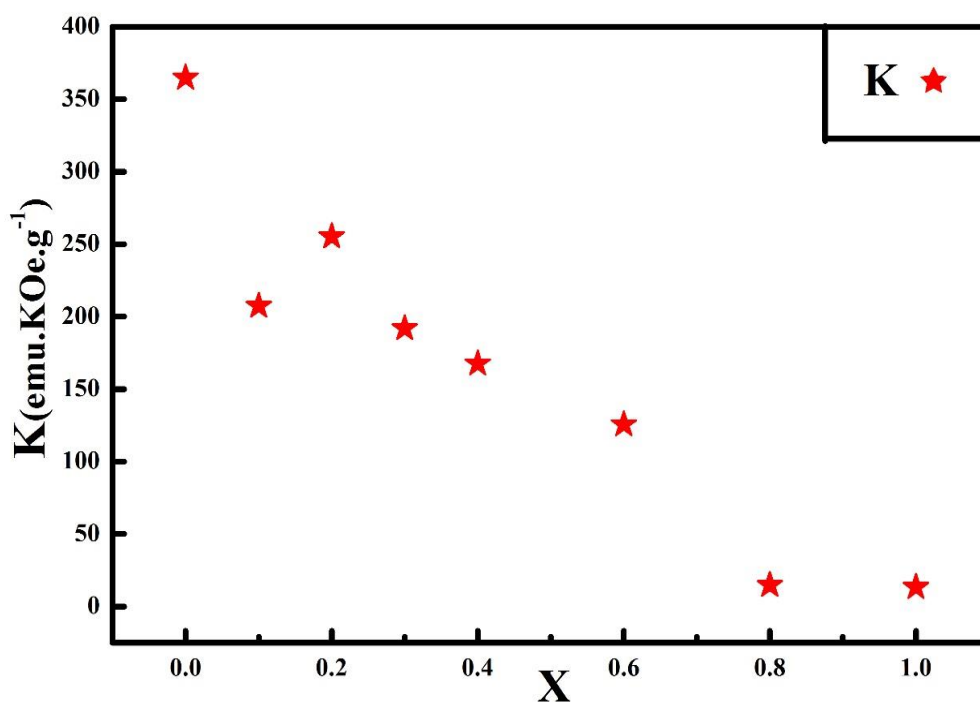


Fig. 10: The variations of K with respect to x values for $PbFe_{12-x}Ni_xO_{19}$ nanoparticles annealed at $800\text{ }^\circ\text{C}$ for 3 h.

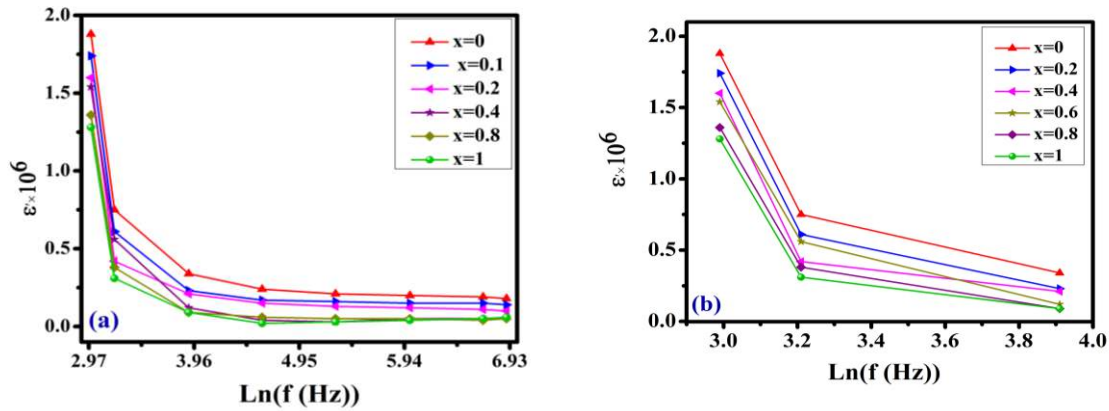


Fig. 11: Variation of the dielectric constant as a function of frequency for $\text{PbFe}_{12-x}\text{Ni}_x\text{O}_{19}$ nanoparticles annealed at 800°C for 3 h with $x = 0.0, 0.2, 0.4, 0.6, 0.8$ and 1 : (a) in the range of all applied frequencies and (b) in the range 20Hz -50Hz.

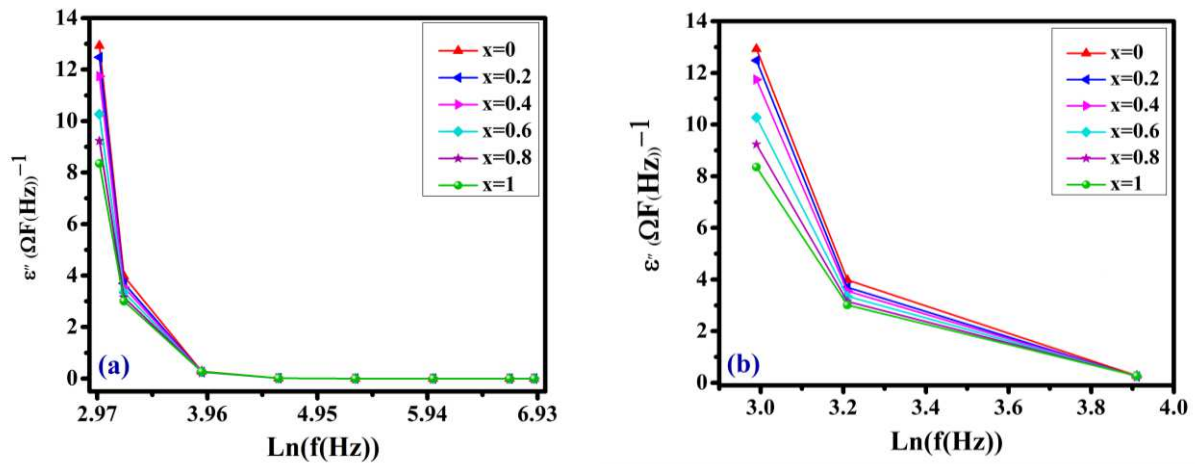


Fig. 12: Variation of the dielectric loss as a function of frequency for $\text{PbFe}_{12-x}\text{Ni}_x\text{O}_{19}$ nanoparticles annealed at 800°C for 3 h with $x = 0.0, 0.2, 0.4, 0.6, 0.8$ and 1 : (a) in the range of all applied frequencies and (b) in the range 20Hz -50Hz.

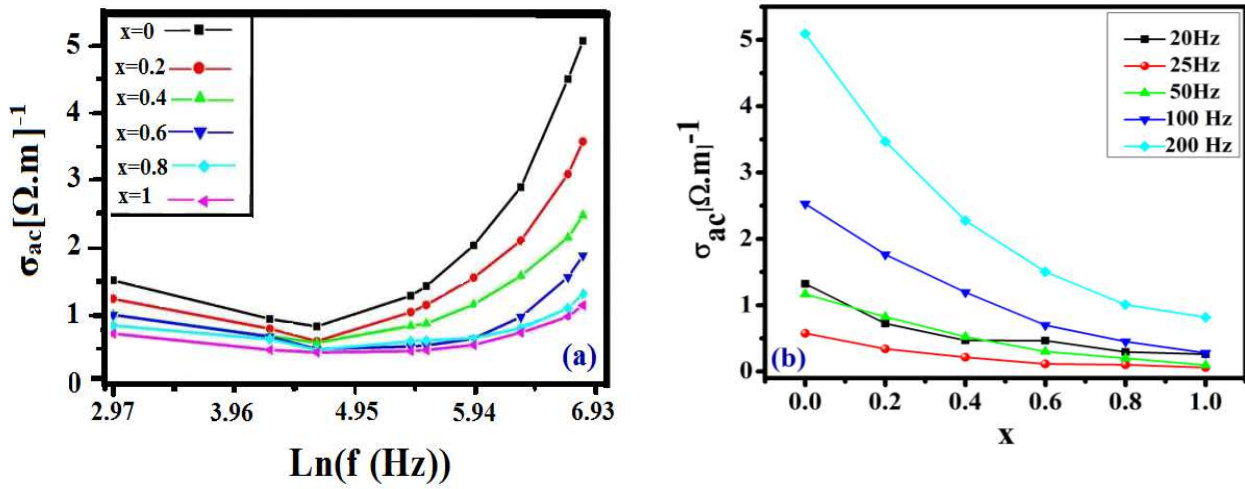


Fig. 13: Variation of ac electric conductivity as a function of frequency for $PbFe_{12-x}Ni_xO_{19}$ nanoparticles annealed at $800\text{ }^\circ\text{C}$ for 3 h with $x = 0.0, 0.2, 0.4, 0.6, 0.8$ and 1: (a) in the range of all applied frequencies and (b) x values with $f = 20\text{Hz}-200\text{Hz}$.

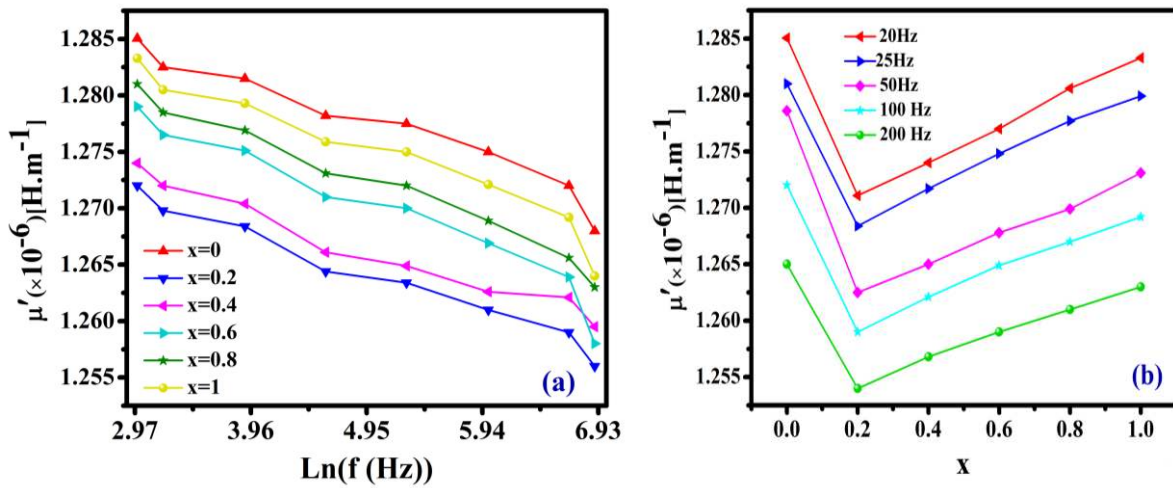


Fig. 14: Variation of μ' as a function of frequency for $PbFe_{12-x}Ni_xO_{19}$ nanoparticles annealed at $800\text{ }^\circ\text{C}$ for 3 h with $x = 0.0, 0.2, 0.4, 0.6, 0.8$ and 1: (a) in the range of all applied frequencies and (b) x values with $f = 20\text{Hz}-200\text{Hz}$.

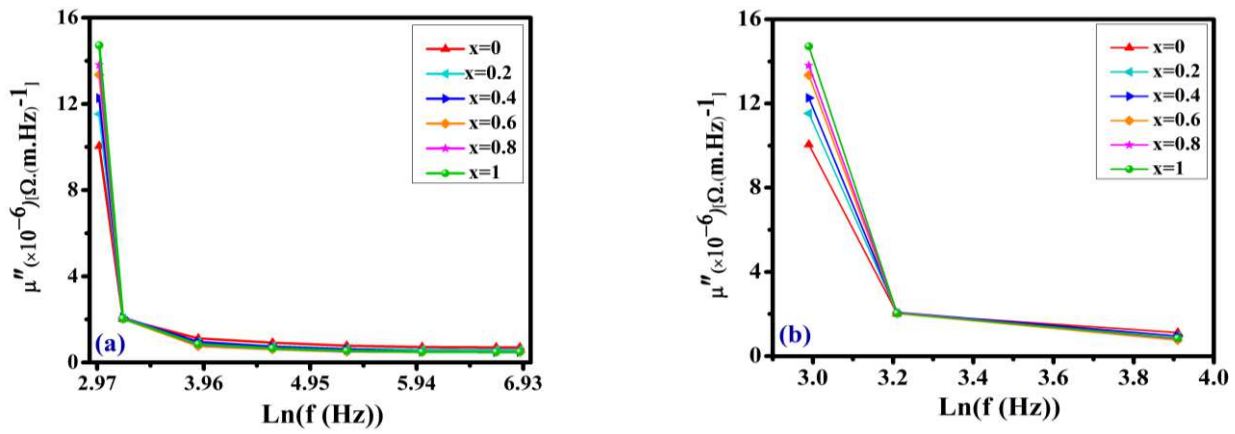


Fig. 15: Variation of μ'' as a function of frequency for $\text{PbFe}_{12-x}\text{Ni}_x\text{O}_{19}$ nanoparticles annealed at $800\text{ }^\circ\text{C}$ for 3 h with $x = 0.0, 0.2, 0.4, 0.6, 0.8$ and 1: (a) in the range of all applied frequencies and (b) in the range 20Hz -50Hz.

Tables

Table 1: The values (a, c), V_{cell} , D, and d_x for $\text{PbFe}_{12}\text{O}_{19}$ nanoparticles annealed at 800 °C for 3 h with $x = 0.0-1$.

x	a(Å)	c(Å)	$\frac{c}{a}$	V_{cell} (Å ³)	D (nm)	d_x (g.cm ⁻³)
0.0	5.859	23.982	4.093	713.429	28	5.479
0.1	5.860	23.971	4.091	713.346	26	5.718
0.2	5.862	23.042	3.931	686.168	28	5.739
0.3	5.862	23.061	3.933	686.258	25	5.738
0.4	5.864	23.031	3.928	686.308	23	5.741
0.5	5.867	23.024	3.924	686.802	21	5.755
0.6	5.860	22.991	3.923	686.680	17	5.737
0.8	5.861	22.734	3.879	684.182	21	5.730
1	5.864	22.173	3.781	660.741	21	5.703

Table 2: The values of M_s , M_r , M_r/M_s , H_c , H_a , H_d , and K for $PbFe_{12}O_{19}$ nanoparticles annealed at 800 °C for 3 h with $x = 0.0-1$.

x	$M_s(\frac{emu}{g})$	$M_r(\frac{emu}{g})$	$\frac{M_r}{M_s}$	$H_c(Oe)$	$H_a(Oe)$	$H_d(Oe)$	$K(\frac{emu}{g}KOe)$
0.0	50.279	29.204	0.581	3609.67	14507	6987	364.69
0.1	40.323	22.235	0.554	2730.78	10283	4593	207.37
0.2	43.401	23.235	0.535	2897.49	11761	5933	255.23
0.3	38.133	21.414	0.561	2732.52	10065	4372	191.90
0.4	38.285	19.589	0.511	1468.20	8663	5605	167.57
0.6	33.642	15.158	0.450	943.65	7457	5492	125.44
0.8	4.230	1.594	0.377	716.53	6952	5460	14.70
1	4.062	1.555	0.383	678.67	6522	5109	13.25

Figures

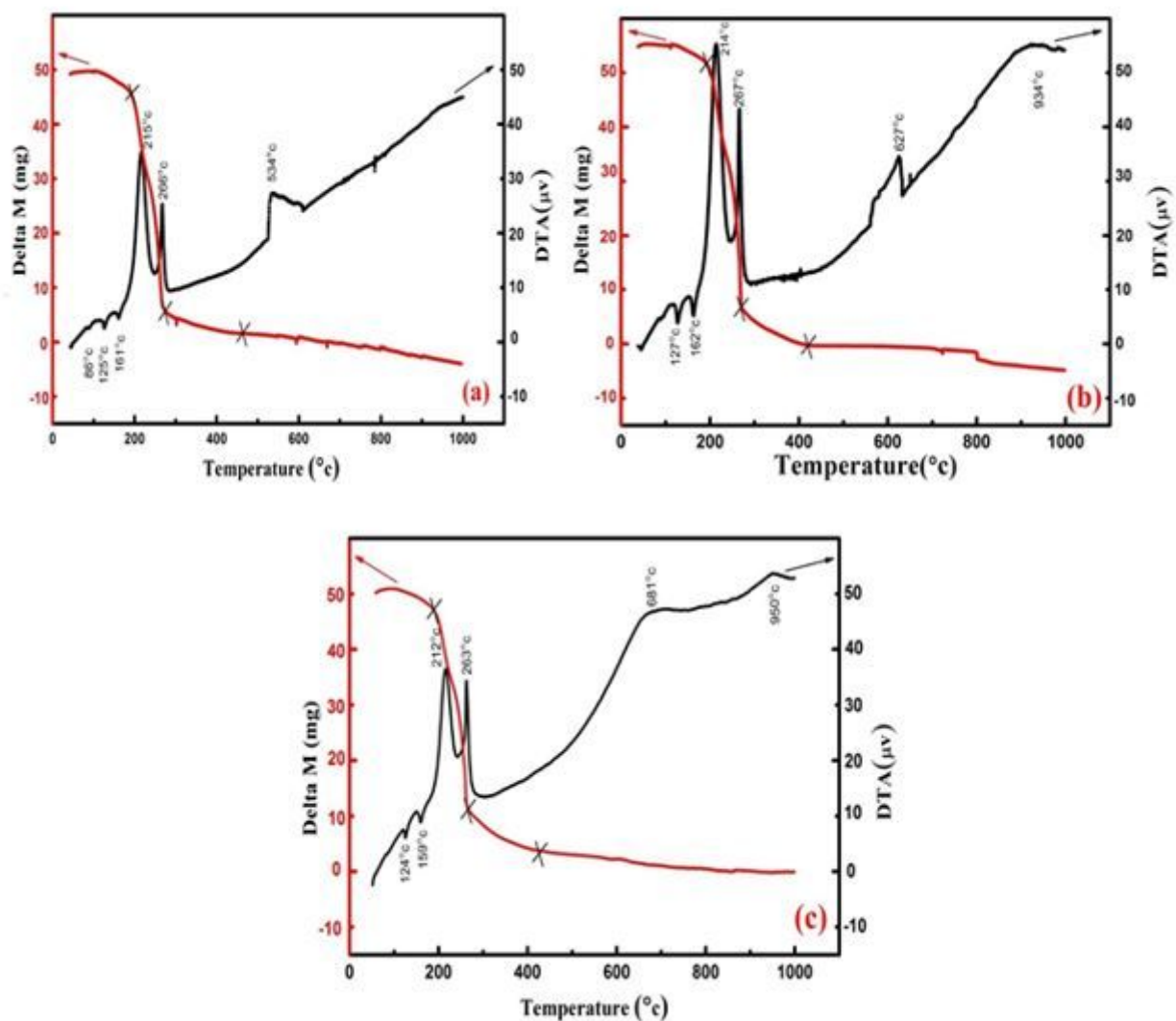


Figure 1

TGA/DTA curves of the dry-gel precursor of $\text{PbFe}_{12-x}\text{Ni}_x\text{O}_{19}$ nanoparticles annealed at 800 °C for 3 h with (a) $x = 0.0$; (b) $x = 0.2$ and (c) $x = 0.6$.

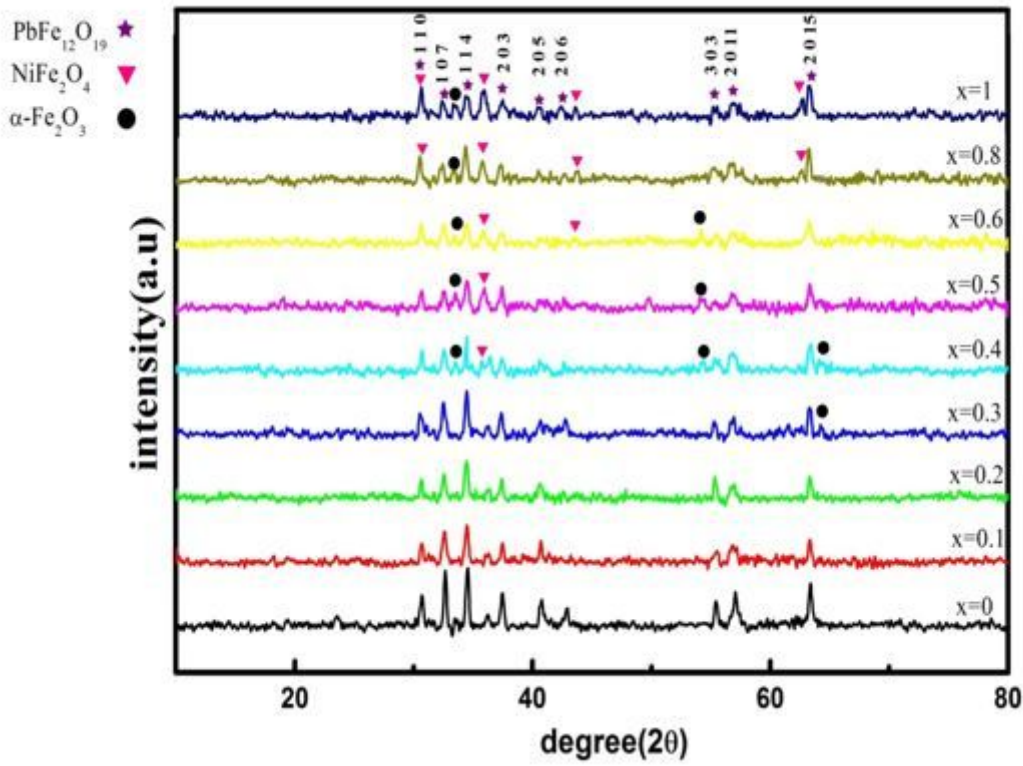


Figure 2

XRD patterns of $\text{PbFe}_{12-x}\text{Ni}_x\text{O}_{19}$ nanoparticles annealed at 800 °C for 3 h with $x = 0.0-1$.

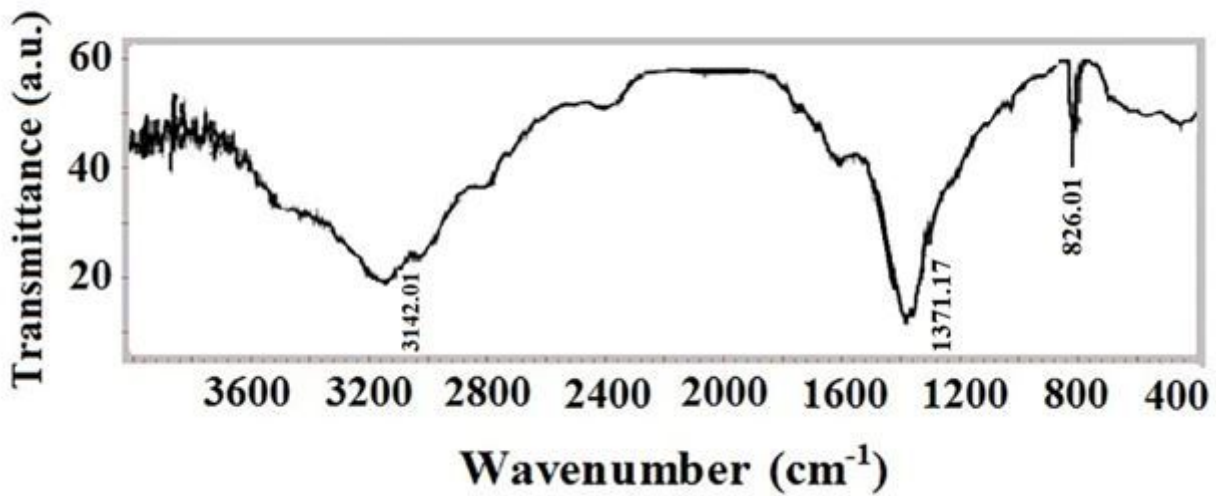


Figure 3

FT-IR pattern of $\text{PbFe}_{12-x}\text{Ni}_x\text{O}_{19}$ nanoparticles dry-gel.

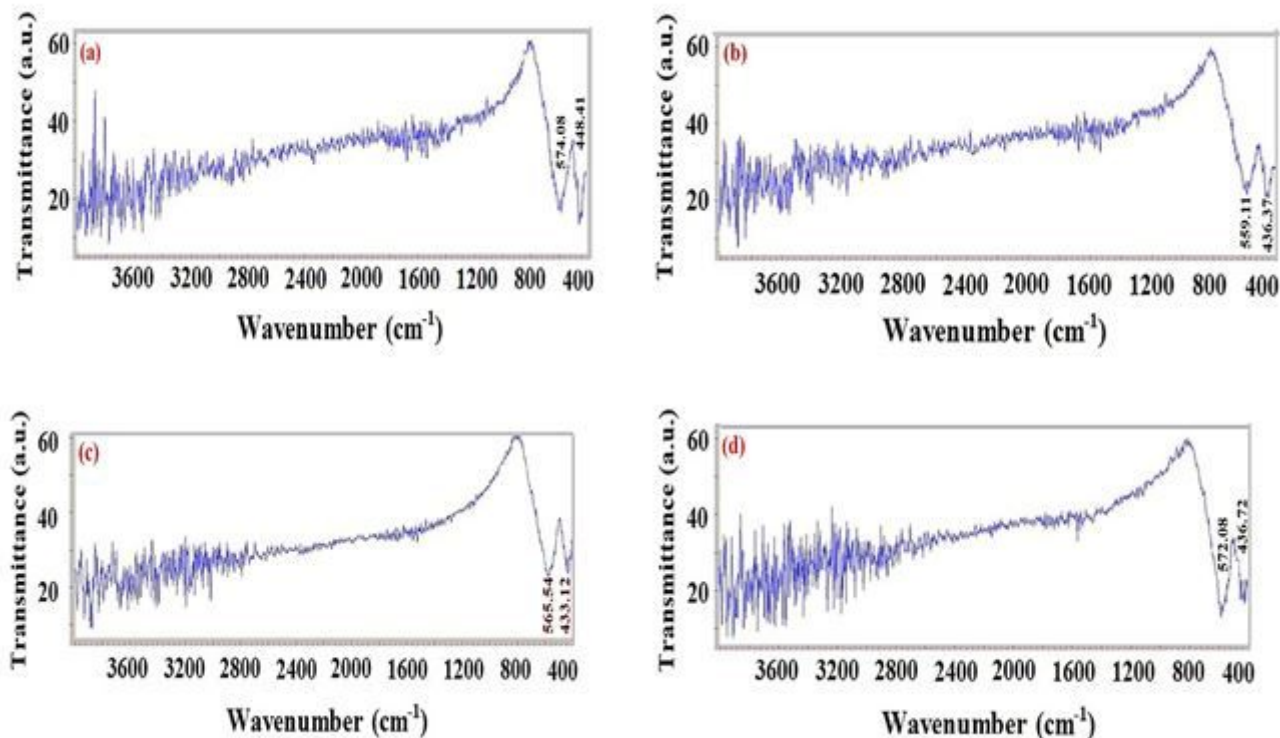


Figure 4

FT-IR patterns of PbFe_{12-x}Ni_xO₁₉ nanoparticles annealed at 800 °C for 3 h with (a) x = 0.0; (b) x = 0.2; (c) x = 0.4 and (d) x = 1.

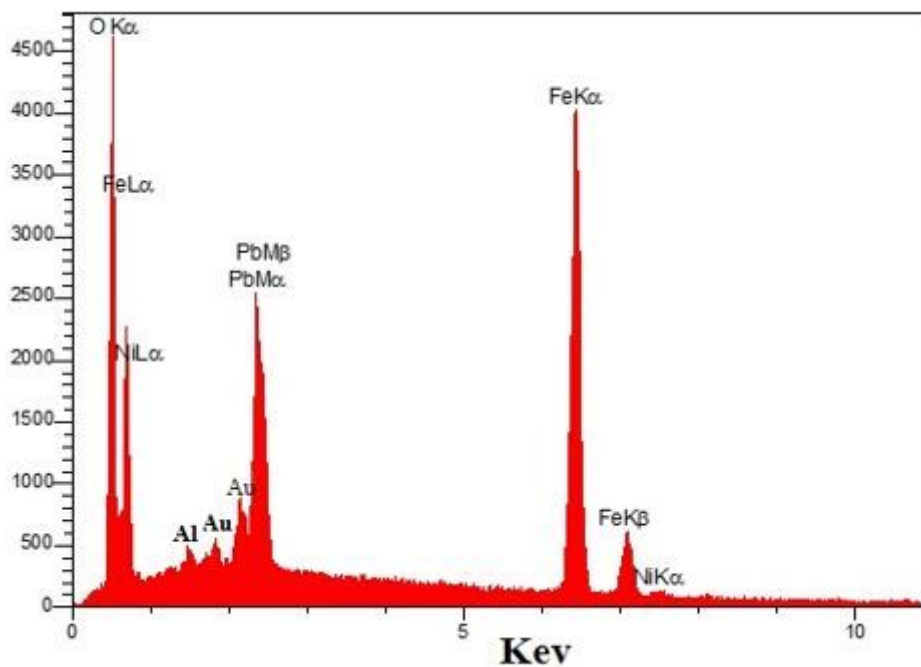


Figure 5

EDX pattern of PbFe_{11.8}Ni_{0.2}O₁₉ nanoparticles annealed at 800 °C for 3 h.

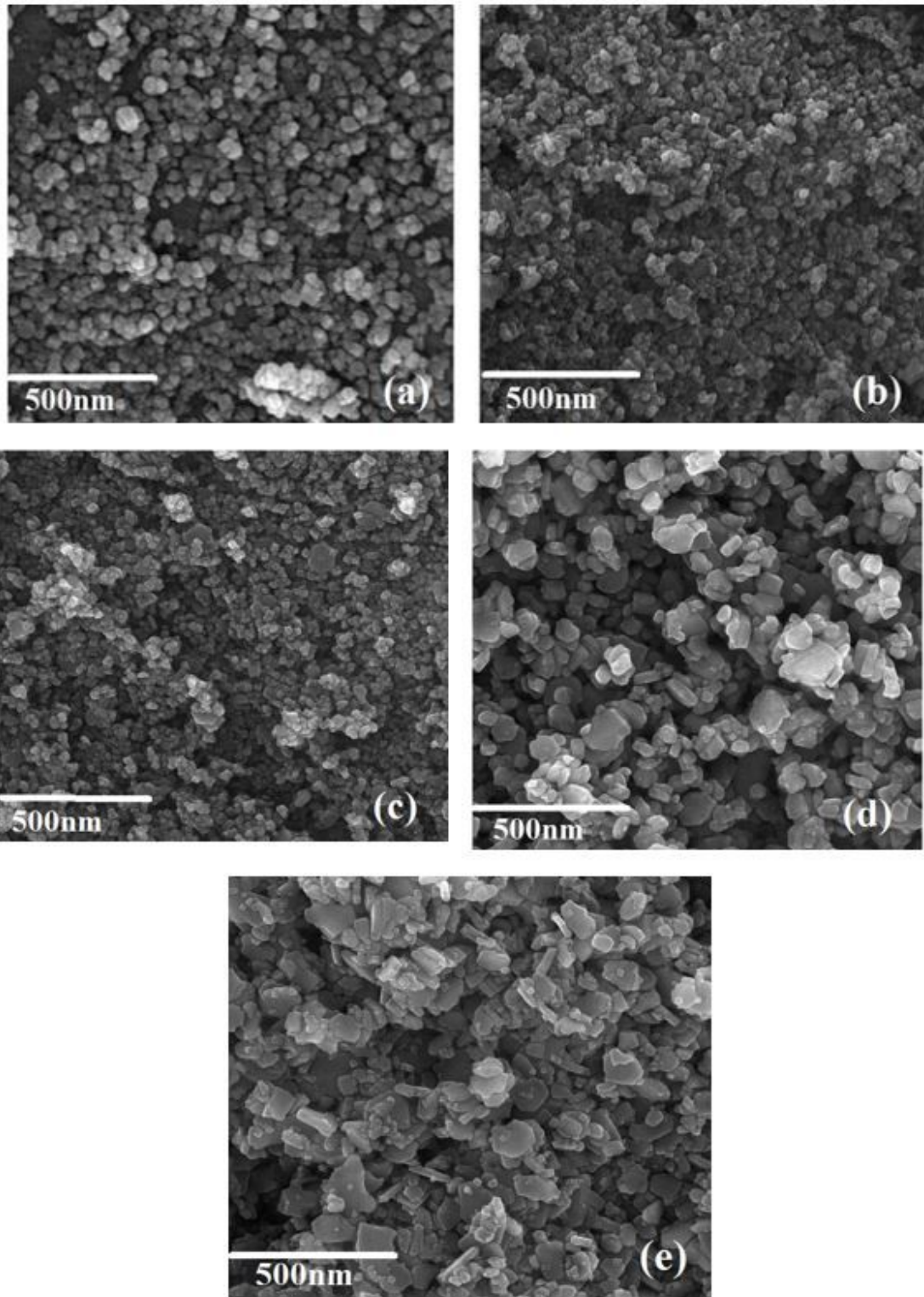


Figure 6

SEM images of $\text{PbFe}_{12-x}\text{Ni}_x\text{O}_{19}$ nanoparticles annealed at $800\text{ }^\circ\text{C}$ for 3 h with (a) $x = 0.0$, (b) $x = 0.2$, (c) $x = 0.4$, (d) $x = 0.6$ and (e) $x = 1$.

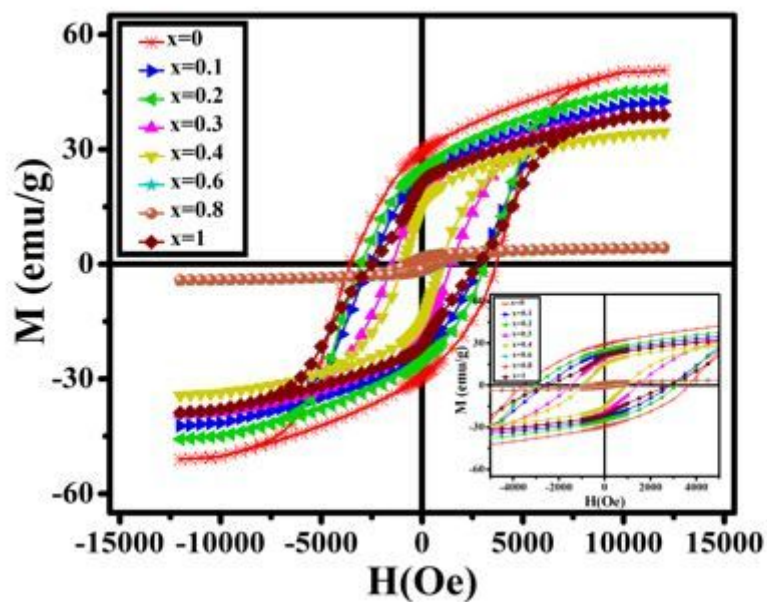


Figure 7

M-H hysteresis loops of $\text{PbFe}_{12-x}\text{Ni}_x\text{O}_{19}$ nanoparticles annealed at 800 °C for 3 h with $x = 0.0-1$.

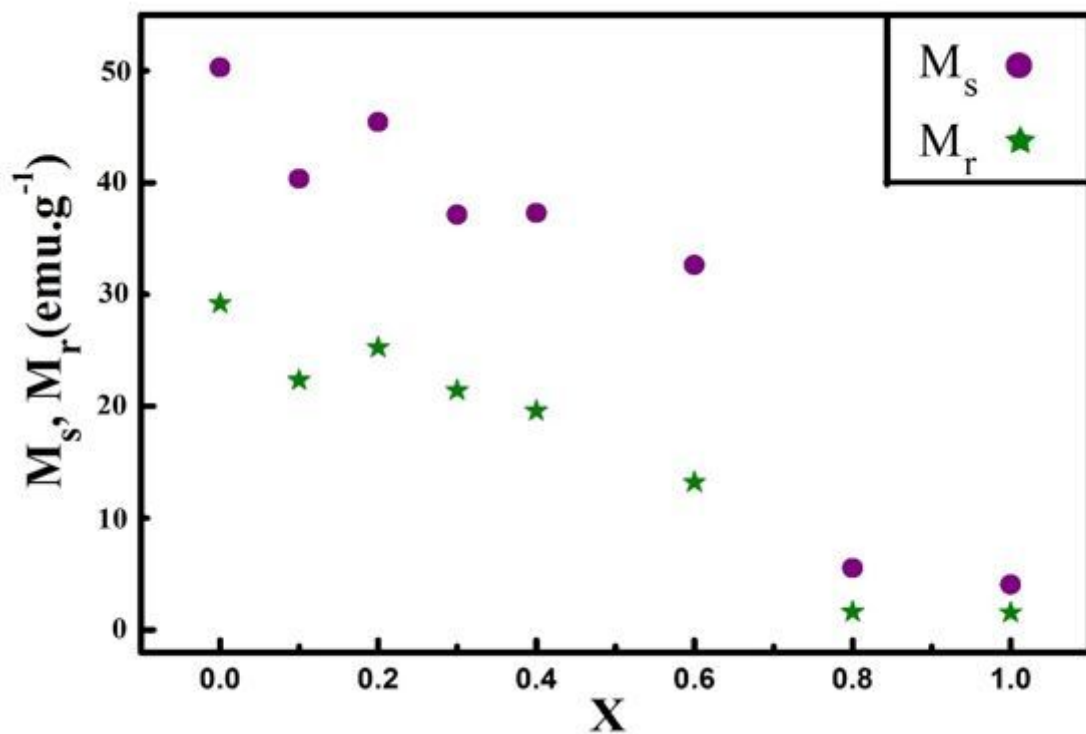


Figure 8

The variations of M_s and M_r with respect to x values for $\text{PbFe}_{12-x}\text{Ni}_x\text{O}_{19}$ nanoparticles annealed at 800 °C for 3 h.

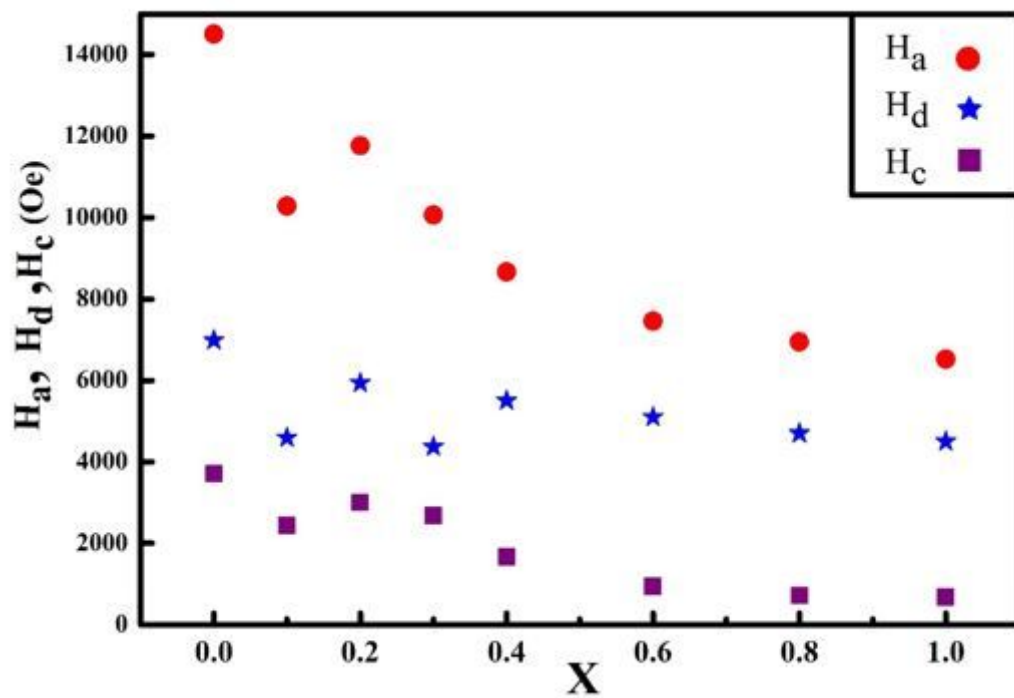


Figure 9

The variations of H_c, H_a and H_d with respect to x values for PbFe_{12-x}Ni_xO₁₉ nanoparticles annealed at 800 °C for 3 h.

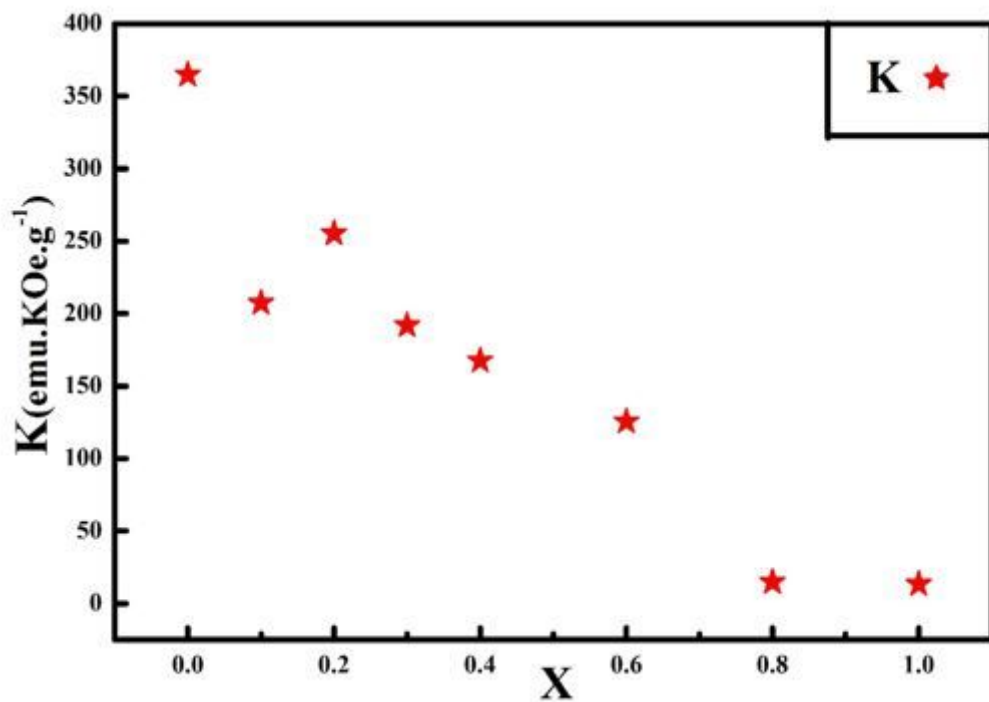


Figure 10

The variations of K with respect to x values for PbFe_{12-x}Ni_xO₁₉ nanoparticles annealed at 800 °C for 3 h.

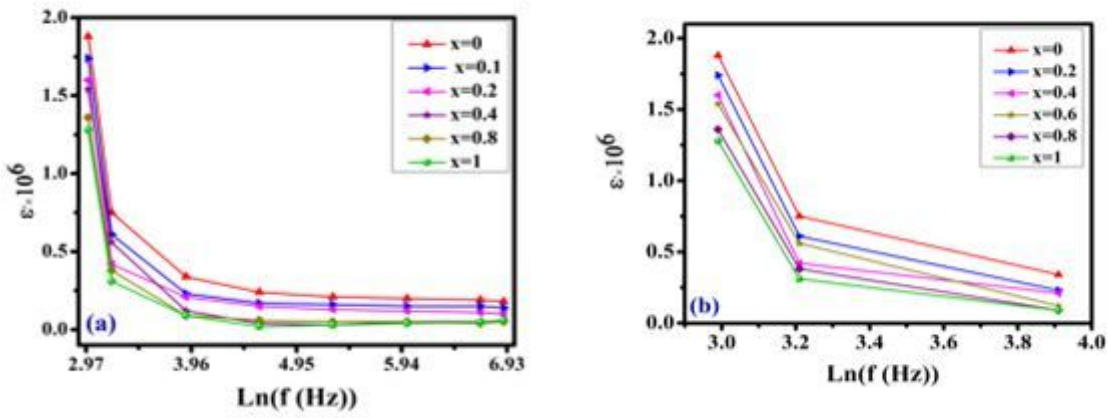


Figure 11

Variation of the dielectric constant as a function of frequency for $\text{PbFe}_{12-x}\text{Ni}_x\text{O}_{19}$ nanoparticles annealed at 800 °C for 3 h with $x = 0.0, 0.2, 0.4, 0.6, 0.8$ and 1: (a) in the range of all applied frequencies and (b) in the range 20Hz -50Hz.

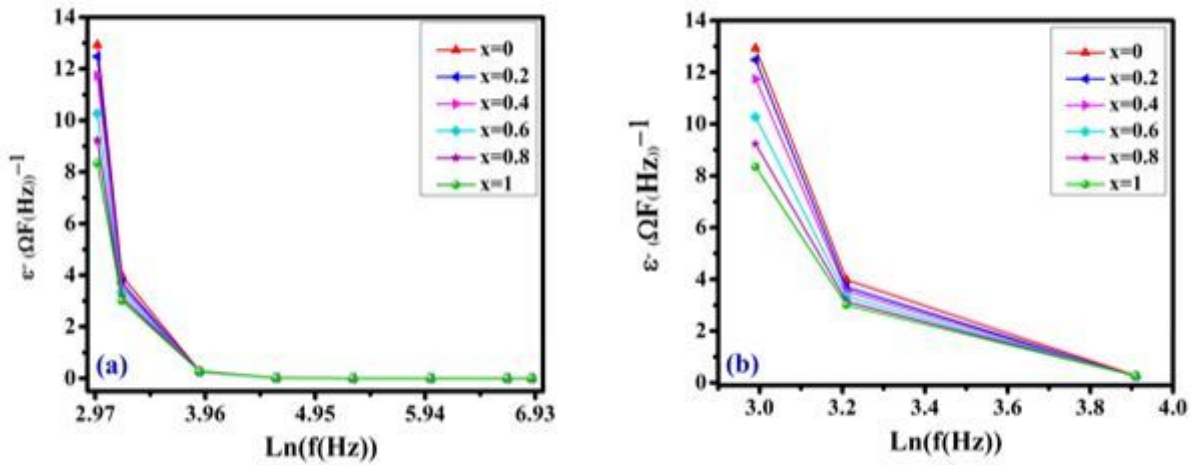


Figure 12

Variation of the dielectric loss as a function of frequency for $\text{PbFe}_{12-x}\text{Ni}_x\text{O}_{19}$ nanoparticles annealed at 800 °C for 3 h with $x = 0.0, 0.2, 0.4, 0.6, 0.8$ and 1: (a) in the range of all applied frequencies and (b) in the range 20Hz -50Hz.

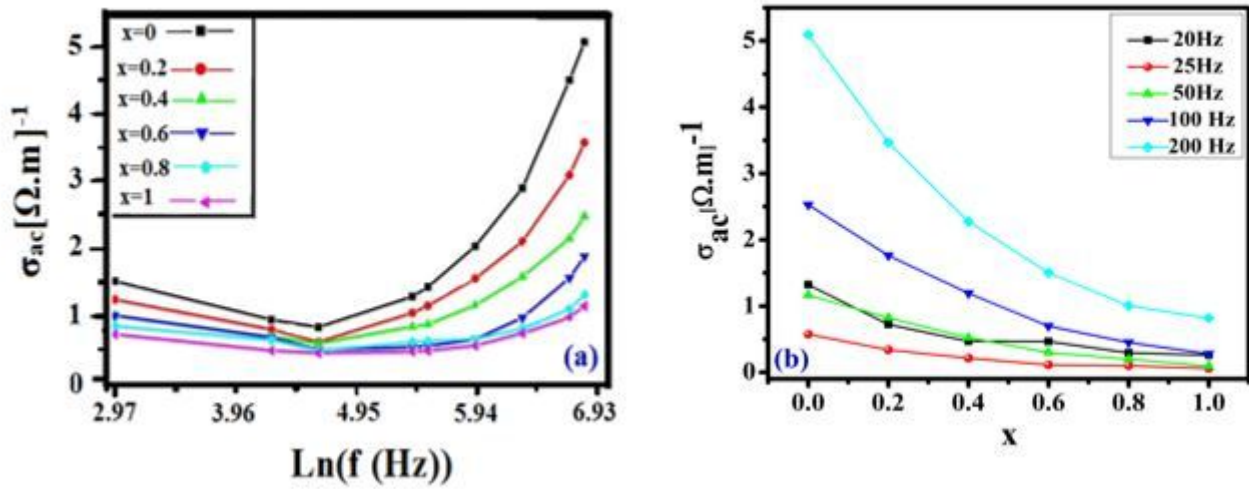


Figure 13

Variation of ac electric conductivity as a function of frequency for $\text{PbFe}_{12-x}\text{Ni}_x\text{O}_{19}$ nanoparticles annealed at 800°C for 3 h with $x = 0.0, 0.2, 0.4, 0.6, 0.8$ and 1: (a) in the range of all applied frequencies and (b) x values with $f = 20\text{Hz}-200\text{Hz}$.

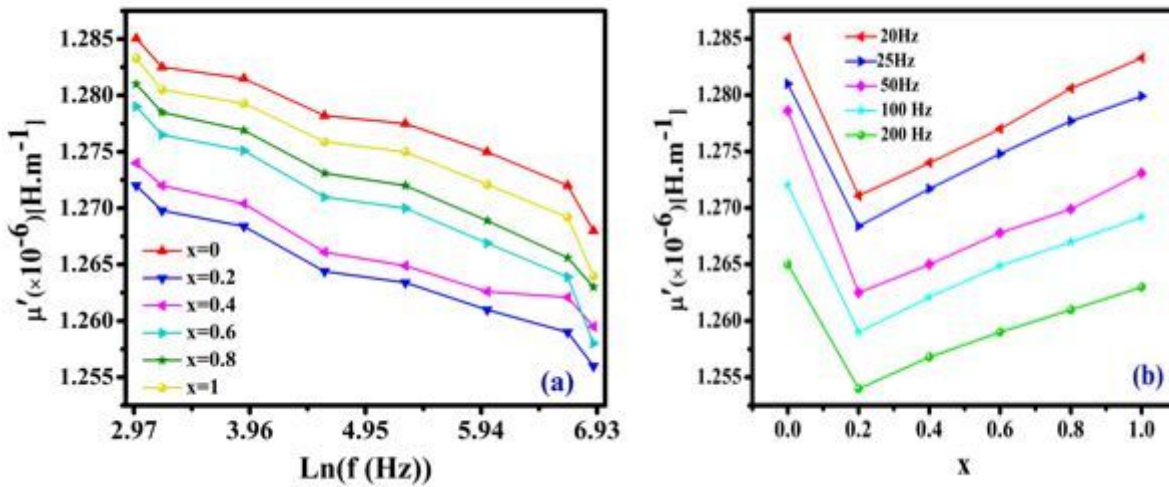


Figure 14

Variation of μ' as a function of frequency for $\text{PbFe}_{12-x}\text{Ni}_x\text{O}_{19}$ nanoparticles annealed at 800°C for 3 h with $x = 0.0, 0.2, 0.4, 0.6, 0.8$ and 1: (a) in the range of all applied frequencies and (b) x values with $f = 20\text{Hz}-200\text{Hz}$.

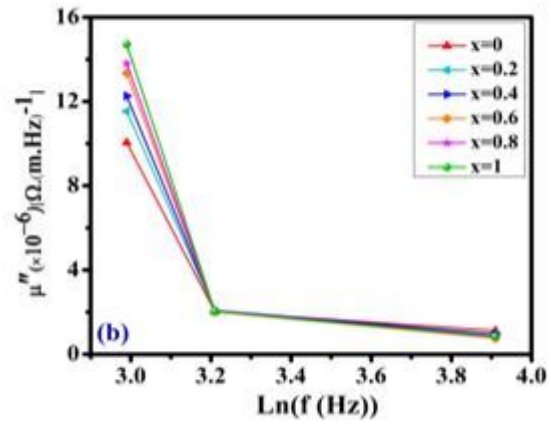
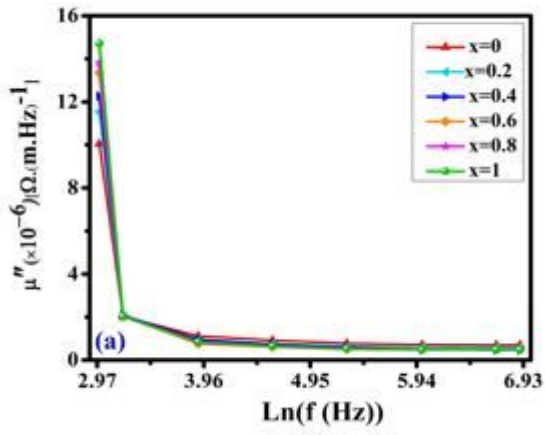


Figure 15

Variation of μ'' as a function of frequency for $\text{PbFe}_{12-x}\text{Ni}_x\text{O}_{19}$ nanoparticles annealed at $800\text{ }^\circ\text{C}$ for 3 h with $x = 0.0, 0.2, 0.4, 0.6, 0.8$ and 1 : (a) in the range of all applied frequencies and (b) in the range $20\text{Hz} - 50\text{Hz}$.